Image-based characterization of the bubbly shock wave generation and evolution in aviation fuel cavitation

Igal Gluzman [*] and Flint O. Thomas [†]
Institute for Flow Physics and Control, University of Notre Dame, Notre Dame, Indiana 46556, USA

(Received 28 October 2021; accepted 2 August 2022; published 30 August 2022)

Unsteady shock wave propagation and generation mechanisms in aviation fuel cavitation are experimentally characterized in a planar converging-diverging nozzle geometry via high-speed digital imaging and a signal processing technique that we denote as enhanced gradient shadowgraphy. Two fuels, JP-5, and JP-8, in two different flow cavitation regimes were studied: (1) aerated cavitating flow, where air microbubbles are injected into the flow at the nozzle inlet, and (2) nonaerated cavitating flow, where the flow evolved into the two-phase cavitating flow without bubble injection. For a sufficiently low range of imposed nozzle pressure ratios, gaseous cavitation led to choked flow for each working fluid. Two independent sustained mechanisms responsible for shock wave generation in the diverging section of the nozzle have been observed and characterized in the choked flow regime. The first mechanism exists only in the aerated case due to the injected bubbles. The second mechanism exists in both aerated and nonaerated cases and resulted in weaker shock waves than in the first case. This is related to the shed cavity clouds from a sheet cavity attached to nozzle sidewalls. More violent collapse events and stronger shock wave emissions were observed for aerated JP-5 than JP-8 due to the first mechanism. Detailed quantitative data are obtained to characterize shock wave intensity and velocity in aerated flow regimes under different bubble injection rates, nozzle back pressures, and void fractions. A strong similarity is obtained between shock speeds from our experimental data and the nonlinear solutions of the governing equations for nonbarotropic homogeneous flow. Results from the study shed some light on the complex physics of unsteady fuel cavitation phenomena and may lead to improved design of fuel system components, which suffer from system performance degradation due to the damaging impact of these shock waves.

DOI: 10.1103/PhysRevFluids.7.084305

I. INTRODUCTION

Understanding the fundamental physical mechanisms involved in shock wave generation in internal cavitating flows of hydrocarbon fuels has high importance in many practical applications. The cavitation and the resulting shock waves in an aircraft fuel system can lead to unexpected material degradation and failure of fuel system components [1]. These systems are often characterized by complex internal flow geometries that include narrow flow paths and sharp turns, which give rise to large decreases in static pressure that can lead to gaseous and/or vaporous cavitation [2].

The flow field within realistic component geometries, such as fuel pumps, injectors, and various hydraulic systems, is difficult to examine due to limited optical access, small characteristic lengths, and complex geometries. Thus, experimental investigations are primarily performed with larger

[*]Current address: Faculty of Aerospace Engineering, Technion–Israel Institute of Technology, Haifa 32000, Israel, igluzman@nd.edu, igal.gluzman@technion.ac.il
[†]Flint.O.Thomas.1@nd.edu

scale transparent generic geometries for the purpose of providing an improved understanding of the underlying cavitation mechanisms. For example, a generic converging-diverging (CD) nozzle geometry captures much of the essential cavitation mechanisms that play a crucial role in these systems. A vast literature is available regarding CD nozzles, which allows isolating these mechanisms in a well-understood configuration.

The most severe cavitation noise and erosion in external and internal flows are produced when many bubbles collapse close to each other, which may result in severe damage on the solid surface [3]. The collapse of a cloud of bubbles involves the formation and inward propagation of a shock wave [4]. The geometric focusing of this shock at the center of the cloud enhances the noise and damage potential associated with cloud collapse [5]. This type of cavitation is commonly referred to as cloud cavitation [6]. Cloud cavitation is a form of partial cavitation where vapor/gaseous clouds are periodically shed from the main cavity [7]. Cloud cavitation has been investigated extensively in external flows, such as flow around hydrofoils [8–11], and internal flows such as water jet pumps [12,13], CD nozzles [14–17], and wedges [18]. The periodic cloud shedding process is initiated by the upstream motion of a disturbance, which can be either a thin liquid film underneath the cavity (reentrant jet) or a bubbly condensation shock [14,19].

In internal flows, the mechanisms of cavity cloud collapse have been observed for different cavitating flow regimes. The severity of collapse events and bubbly shock wave emissions grows with an increase in void fraction. One of these flow regimes is the shed cavity clouds from a sheet cavity attached to the nozzle sidewalls, which is referred to as nonaerated cavitation. The cavity shedding cycle process has been the subject of many studies, and details can be found in [6]. In the nozzle, the sheet cavity inception starts from the throat exit and grows with downstream distance. The created reentrant jet at the attached cavity's trailing edge creates a stagnation point that pushes the fluid beneath the cavity and its inception surface, which triggers the separation of a swirling cavity cloud from the main body of the attached cavity that is shed and advected farther downstream [15]. The rapid pressure increase in the divergent section of the nozzle triggers the collapse of the shed vapor cloud cavity, while the attached cavity begins to grow again and the cycle is repeated. In bubbly flows, it was also demonstrated that the shedding mechanism can be triggered by bubbly shock waves rather than the reentrant jet [14].

The cloud cavitation has an extremely violent behavior at high void fractions in cavitating flows due to the enhancement of the pressure waves when bubbles collapse. The increase of void fraction can occur when microbubbles are injected into the existing nonaerated cavitating flow, and this is denoted as the aerated cavitation regime. The aerated flow regime serves as a somewhat idealized case in which experimental data can be obtained and compared with nonlinear equation solutions to study the behavior of shock waves and the sonic speed in a bubbly cavitating flow [20–23]. Moreover, it allows creating a precise initial void fraction by controlling the rate of injection of noncondensable gas microbubbles.

In aerated cases, the injection of noncondensable gas was found to be significant in its effect on cavity flow compared to the effect of dissolved gas, in which content variation was found to be less significant in affecting the dynamics of natural cavitation in water [24,25]. Dong and Su [26] showed that the aeration phenomenon gives rise to a remarkable increase in the compression waves and shock waves in the aerated cavitation region compared to the nonaerated case. In [15] three different cavitation regimes in venturi nozzles have been studied (cloud cavitation, quasisupercavitation, and supercavitation), which have been further aerated by injecting air bubbles. They showed that even for the smallest amount of injected air on the order of 1% by volume, this caused drastic effects on the cavitation dynamics, which modified the characteristic lengths and frequencies of these regimes. The injected air bubbles flowing in the nozzle diverging section zone expand their volume, and at a particular moment, they break up into tiny bubbles. Some of them are advected downstream with the flow, while others follow the reentrant jet at the main cavity closure region. As a result, the upper cavitating sheet is extremely disturbed by the bubble that leads it to break up, and no periodic detachment can be observed for this upper sheet. At the same time, a periodic cycle is still present on the upstream side. In further studies, a noncondensable gas presence increase was shown to have a stabilizing effect on the cavity being formed [27], leading to suppression of cavitation-induced unsteady pressure fluctuations and transportation of bubbly shocks [28], suppressing the low-frequency vortex shedding [29] and sustaining cavitation through an efficient attraction of nuclei [30].

Relatively few studies can be found in the open literature involving fundamental aspects of cavitation in hydrocarbon fuels. The ability to model aviation fuel cavitation is challenging due, in part, to the fact that fuels are a mixture of hundreds of hydrocarbons as well as additives for particular applications [31,32]. Furthermore, their dissolved noncondensable gas content varies considerably with storage history. These factors make their properties challenging to determine for modeling and simulations. It has been clearly demonstrated that the physics of aviation fuel cavitation is different from water as observed in [2,33,35]. In more detail, the authors in [33] performed a set of benchmark experiments to determine the properties that govern polytropic and diffusional processes in aviation fuel (JP-8), dodecane (which served as a single-component hydrocarbon surrogate of JP-8), and distilled water. Water served to provide a baseline for comparison with the other fluids. These include the polytropic constant, the diffusion coefficient, Henry's law constant, and the study of the subatmospheric pressure's effect on these three properties. It was shown that the solubility of gases in JP-8 is seven times higher than in water, and the cavitation mechanism observed in the CD nozzle experiments was gaseous, which results in cavity cloud formation and more violent bubbly shock and collapse events [2]. The authors in [2] noted that even for cases where the static pressure dropped below 0.1 of the atmospheric pressure, this was still above the JP-8 liquid vapor pressure. In their study, detailed pressure measurements were obtained in a CD nozzle, and qualitative information was obtained from high-speed imaging techniques.

In [2,34,35] a controlled quantity of microbubbles was injected into a transparent venturi nozzle to study its effects on cavitation in the cases of both water and aviation fuel. The authors in [34] developed a steady, barotropic, quasi-one-dimensional fuel cavitation model in a generic CD nozzle geometry. The analytical model gave rise to a standing bubbly shock in the divergent portion of the nozzle. As shown in Fig. 1, the barotropic model fails to reproduce the more gradual pressure rise observed in CD nozzle cavitation experiments for JP-8 fuel at different nozzle inlet-outlet pressure ratios. This disparity between the predictions from the steady model and experiment suggests the importance of unsteady mechanisms as was shown in [21,36], where the effects of bubble dynamics give rise to traveling unsteady bubbly shock waves and were found to play a significant role in the behavior of cavitating flows, even in the mean. In [2,35], the experimental effort has also advanced our understanding of the considerable differences between cavitation in water, dodecane, and JP-8 aviation fuel. These differences are not subtle. In the water case, the bubble growth starts at nucleation sites near the throat with packets of initially spherical bubbles that grow quickly and coalesce into large vaporous voids. These subsequently undergo a rather sudden collapse in the diverging portion of the nozzle across a well-defined standing bubbly shock wave. In the JP-8 fuel and dodecane cases, the appearance of a visually obvious bubbly standing shock is absent. In fuel, the initial bubble growth phase appears to be followed by a nearly homogeneous bubbly flow that seems to persist to the nozzle exit (as shown in images in [2, Fig. 6]. We will show in the current study that once the bubble cloud experiences growth, a sudden collapse follows, and associated time-dependent shock wave emission occurs in aviation fuels. In previous works, the traveling bubbly shock wave creation mechanism and subsequent evolution in aviation fuels were not fully captured, and several open questions remain. There is a lack of experimental data and validations focusing on the transient formation and propagation of bubbly shocks in hydrocarbon fuels.

In this work, our goal is to study the generation and propagation of bubbly shock waves in aviation fuel cavitation in a generic CD nozzle geometry. We particularly focus on aerated cavitation, where the most aggressive cavity cloud collapse is observed. Our study is focused on JP-5 and JP-8 fuels, which are those most commonly used by the U.S. military. These share similar properties, such as the nominal vapor pressure, $p_v = 1.5$ and 4 kPa at 80 °C, for JP-5 and JP-8, respectively [31]. The experimental CD nozzle geometry with the vacuum-driven blowdown setup that is used in this investigation is comparable to that used in [2]. Two different flow regimes were

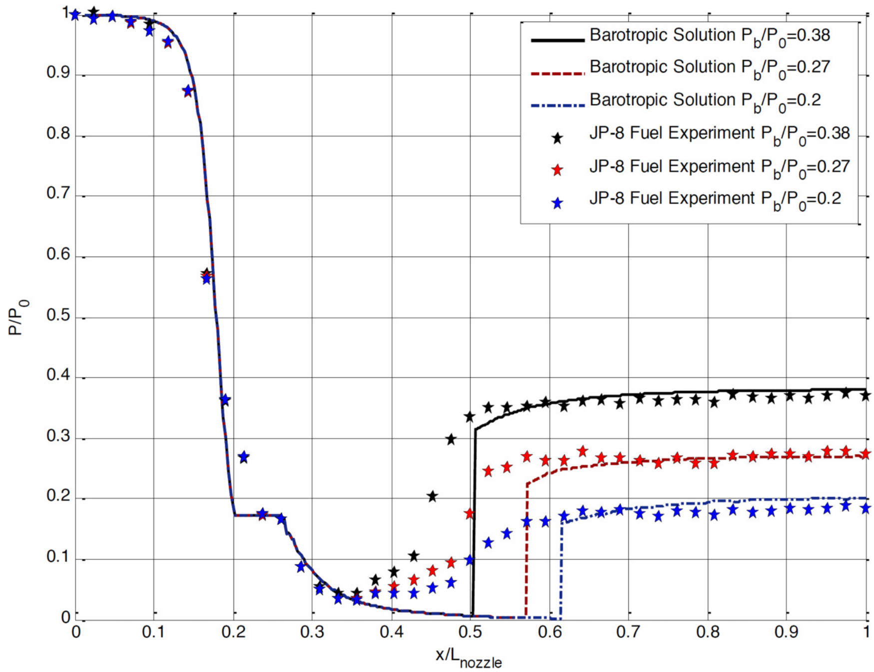

FIG. 1. Barotropic cavitation model predictions and experimental measurements of nozzle mean centerline static pressure distribution in choked flow of JP-8 at different nozzle outlet-inlet pressure ratios P_b/P_0 (for inlet void fraction $\alpha_0 = 0.02$). Reprinted from Dorofeeva *et al.* [34, Fig. 15] with permission from the authors.

studied: (1) aerated cavitating flow, where microbubbles were injected into the flow at the inlet of the nozzle, and (2) naturally occurring nonaerated cavitating flow, where the flow evolved into the two-phase cavitating flow without bubble injection. In both cases for a sufficiently low range of imposed back pressures, gaseous cavitation led to choked flow for both working fluids. These two regimes have been studied in the past and serve as a convenient ground to characterize the cavity collapse and bubbly shock wave behavior in aviation fuels.

The contribution of this work is twofold. First, we characterize two plausible independent, sustained mechanisms likely responsible for bubbly shock wave generation in the diverging section of the CD nozzle that are observed in the choked flow regime. The first mechanism exists only in the aerated case due to the injected bubbles. The second mechanism exists in both aerated and nonaerated cases and results in weaker shock waves than in the aerated case. It is related to the shed swirling cavity clouds from the central cavitation region that is sustained and originates from the nozzle sidewalls. More violent collapse events and stronger shock wave emissions will be shown to exist for aerated JP-5 than JP-8 due to the first mechanism. Second, we provide unprecedented quantitative data on bubbly shock wave emission and their propagation characteristics via a high-speed image processing technique, which we denote as the enhanced gradient shadowgraphy method. The method is used to enhance phase changes and the presence of bubbly shock waves by processing the images obtained via a shadowgraphy imaging setup without the need for experimental setup modification. Our findings show a substantial similarity between the experimentally measured shock speeds and the predictions from nonlinear solutions of the governing equations. Results from our study provide clarification regarding the underlying physical processes of fuel cavitation that were partially captured in Refs. [2,35], which relied on dynamic and static pressure data for quantitative assessment. Our experimental results may be used to validate modeling approaches.

The experimental facility and parameters and the enhanced gradient shadowgraphy technique are presented in Secs. II and III, respectively. Mechanisms responsible for bubbly shock wave

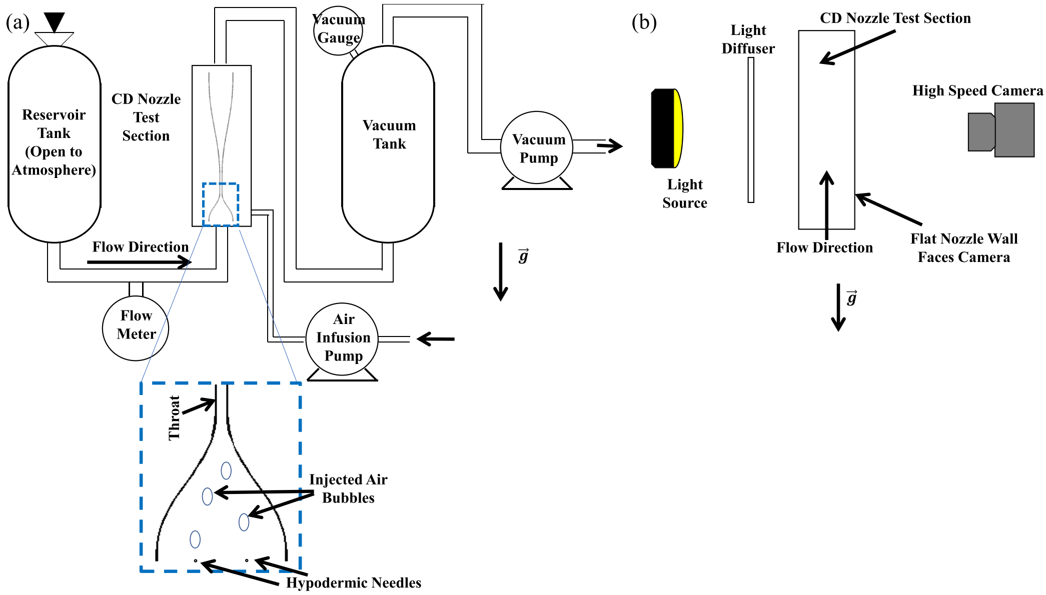

FIG. 2. Experimental setup: (a) cavitation facility with microbubble injection. (b) High-speed imaging setup. Reprinted from Waldrop and Thomas [35, Fig. 1] with permission from the authors.

generation and the detailed quantitative data that characterizes their evolution are provided in Sec. IV. Finally, concluding remarks and directions for future work are discussed in Sec. V.

II. SETUP AND TECHNICAL DETAILS

The experimental setup is shown schematically in Fig. 2. The reader will find a detailed description of the facility in Refs. [35,37]. Here we provide only essential aspects relevant to the scope of the work to be presented. A transparent plexiglass CD nozzle of rectangular cross section is used and shown in Fig. 2(a). The nozzle has a length of $L = 127$ mm, a maximum cross-stream width, which occurs at the inlet and outlet, of $0.15L$, and a constant spanwise depth of $0.0126L$. The throat has a constant cross-stream width of $0.0126L$ and begins at $x = 0.2L$ and ends at $x = 0.25L$ from the nozzle inlet. The internal nozzle walls are precision machined to assure a hydraulically smooth surface for the considered flow regimes at the surface finish of $4L$ (based on S-22 Microfinish Comparator), which correspond to an average deviation of $0.10\ \mu$m from the mean surface. To eliminate the possibility of a corner in the test section to act as an inception point, the nozzle-wall contour was designed using a fifth-order polynomial fit with first and second derivatives set to zero at the inlet and outlet of the converging and diverging portions to ensure smooth transitions between inlet, throat, and outlet sections. In detail the following polynomial coefficients are used to describe the nozzle cross stream area variation: inlet, $0 < x/L < 0.2$: $A(x)[\mathrm{m}^2] = 0.0000304 - 16.989x^3 + 1003.29x^4 - 15799.8x^5$; throat, $0.2 < x/L < 0.25$: $A(x)[\mathrm{m}^2] = 0.0016^2$; and the outlet, $0.25 < x/L < 1$: $A(x)[\mathrm{m}^2] = -0.0000135941 + 0.00173205x - 0.068191x^2 + 1.18126x^3 - 8.45569x^4 + 21.3057x^5$. Here the x value units in the polynomials are in meters [m]. The nozzle is installed vertically to prevent any buoyancy related preference for cavitation inception from one sidewall or the other. A flat transparent cover plate for imaging is sealed using vacuum paste between mating surfaces. This approach ensures an airtight seal between the nozzle and the surrounding environment.

The nozzle inlet was connected to an upstream fuel storage tank (of 11.36 liters volume) which is exposed to atmospheric pressure. The nozzle outlet was connected to the downstream (18.93

liters volume) vacuum tank. This vacuum-driven-blowdown setup ensures the flow will reach pressures low enough for gaseous cavitation to occur in a lower mass flow rate, which for fuels typically occurs well below atmospheric pressure [31]. We obtained the nozzle inlet (at $x/L = 0$) and outlet (at $x/L = 1$) static pressures using a Setra model 209 pressure transducer with a range of 0 to 101.353 kPa ±0.25% full-scale accuracy, which yields uncertainty in nozzle pressure ratio up to $e_{(p_b/p_0)} = 1.2\%$. The Setra sensors are calibrated using a Dwyer vacuum gauge with a range of 0 to −100 kPa ±1.5% full-scale accuracy, which is also used to obtain the pressure in the vacuum tank. These Setra sensors are also used to obtain time-mean pressure measurements with a streamwise array of 40 static pressure taps evenly spaced along the centerline of the nozzle (for details see [34]), which results in streamwise pressure profiles as shown in Fig. 1. The flow rate is sampled just before the nozzle test section inlet by a TVF-02 Industrial Flow Meter manufactured by Dwyer that is capable of measuring in the range 0–1.25 GPM-H_2O with precision to the second decimal place, which in our case leads to uncertainty of $e_Q = 3.7\times10^{-7}$ m^3/s in volumetric flow units. In the setup, constant back pressure in the vacuum tank can be sustained for a sufficiently large run time. For example, a rise by approximately 1 kPa is observed for a run time of approximately 45 s at a vacuum tank pressure set to 11 kPa, which we verified by observing stable flow rate readings. In comparison, our experiments' high-speed imaging data are acquired within 0.625 s duration, and typically only 125 ms of the data is used for our data postprocessing.

Shadowgraphy is used to visualize and analyze different cavitation regimes. In this approach back-lighting with a light diffuser is used to capture cavitation images with bright liquid phase regions and dark gaseous regions. The images are obtained with a FASTCAM SA1.1 high-speed camera combined with 105 mm/2.8 to 32 telephoto/macrolens manufactured by Kiron. The video recordings are obtained at 8000 frames/s, 1/74 000 s exposure, f-stop 2.8, and resolution 1024×512 for two selected distances of the camera from the CD nozzle: (1) at $8L$ to capture the entire nozzle at resolution of $a = 0.1896$ mm/pixel and (2) at $3L$ to capture the zoomed-in region of the nozzle throat exist to diverging section (in the range: $x/L = 0.2$–0.7) at a resolution of $a = 0.0552$ mm/pixel.

The aerated flow regime, with controlled inlet void fraction α_0, is obtained by injection of a periodic train of micro air bubbles through a pair of blunt-tipped, 33 gauge hypodermic needles flush-mounted upstream of the nozzle inlet (at $x = -0.1L$). Their spanwise separation is set to $0.073L$. The air injection flow rate is controlled using a medical infusion pump. The diameter of the injected air bubbles varied in the range 0.7–1.13 mm, with an average value of 0.94 mm from each injector, which we determined from image recording within the accuracy of our spatial resolution. The injection rate with two injector holes opened gives an inlet void fraction α_0, of 0.012 for choked flow. The lower injection rate is obtained with a single hole injector opening, which gives $\alpha_0 = 0.007$ under the same conditions. The injected bubble size and the determined inlet void fraction were consistent (varied up to 3.0%) between the considered inlet-outlet pressure ratios and liquids in our experiments. For more details on the bubble injection system in our study see [2,37].

Similar to [2], all experiments were repeated within 48 h for each liquid (after filling the reservoir), and different time segments were used for postprocessing from the same experiment. A comparison of the measured pressures, flow rates, and evaluated parameters varied within their measurement uncertainty ranges.

III. ENHANCED GRADIENT SHADOWGRAPHY METHOD

The static pressure jump associated with shock wave passage through a bubbly mixture will precipitate bubble cloud collapse, and the resulting lower void fraction gives rise to an increase in the intensity of the pixels aft of the shock. To enhance the appearance of shock waves in the nozzle and systematically track them for extraction of quantitative data, we developed and employed an image processing technique, which we denote as the enhanced gradient shadowgraphy method. It is illustrated in Fig. 3.

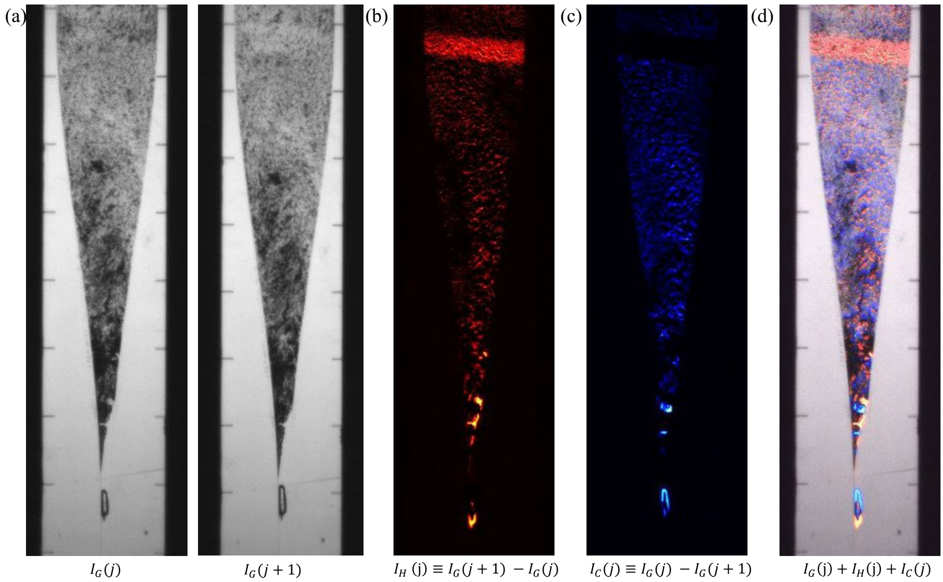

FIG. 3. Enhanced gradient shadowgraphy method based on enhancement of image intensity changes. (a) Two consecutive raw frames, $I_G(j)$ and $I_G(j+1)$. (b) Hot colormap, $I_H(j)$: magnitude of intensity increase (pixel becomes brighter). (c) Cool colormap, $I_C(j)$: magnitude of intensity decrease (pixel becomes darker). (d) Superposition of frame $I_G(j)$ with colored fields $I_H(j)$ and $I_C(j)$.

With this technique, a temporal gradient of the recorded frames enhances the pixel intensity changes. A positive change in intensity is defined as an increase in pixel brightness (corresponding to a reduction in void fraction). We obtain this by subtraction from a given frame j its previous one, $j-1$. Similarly, we obtain a negative change in pixel intensity (corresponding to an increase in void fraction) by subtraction from a given frame j the following frame $j+1$. The resulting fields are denoted by hot- and cool-colored images in Figs. 3(b) and 3(c), respectively. Superposition of the original frame with its positive and negative pixel intensity changes are shown in Fig. 3(d). This superposition holds for sufficiently small time differences between the frames (which in our case is 0.125 ms (several orders of magnitude less than the timescale of the kinematics of the bubbles and bubbly shock waves). The illumination was highly uniform and consistent between our experiments. Also, we made sure that the time interval between consecutive frames is short enough such that when we subtract from each frame its consecutive frame, we eliminate the offset that may vary between different studied cases due to different illumination conditions and cavity populations. One can see from Fig. 3(d) that this enhanced gradient shadowgraphy method captures the phase changes and the bubbly shock waves. The bubble/cavity cloud passes through the liquid and results in a phase change to gas, which results in a pixel intensity decrease and is shown by cool coloring at its downstream (top) edge, whereas phase change to liquid results in an increase of intensity at the cavity/bubble upstream (bottom) edge (denoted by hot coloring). The bubble cloud collapse event and the emitted bubbly shock waves lead to a rapid increase of pixel intensity, denoted by bright hot coloring. The bubbly shock waves give rise to a distinct propagating wave front. In this nozzle setup, passing bubbly shocks were captured in dodecane by computing a positive time derivative of pixel saturation between subsequent frames (denoted by hot coloring in our study), for which dynamic pressure measurements (using Specialties model EPIH 37B pressure transducers with a stated accuracy of ±0.25%) are also obtained and reported in [35]. It was shown that, as the shock front passes bubbles and causes them to collapse, that is translated to a pixel intensity increase and is also observed as a very large pressure pulse [5]. The average value of the shock magnitude (jump in pressure) at $x/L = 0.5$ is documented to be 47.7 kPa (from $\approx$ 22 kPa up to $\approx$ 70 kPa) for $p_b/p_0 = 0.47$ and 36.6 kPa (from $\approx$ 14 kPa up to $\approx$ 51 kPa) for aerated dodecane flow at $p_b/p_0 = 0.36$. The authors in [35] also used 20 s of pressure time-series data sampled at 102.4 kHz to obtain fully converged shock statistics. The obtained histograms of shock emission frequency resulted in bimodal distributions (the histogram plots provided in [35, Fig. 6]), showing that each of these modes occurs at a harmonic of the bubble injection frequency. As will be discussed in detail in the following section, our imaging analysis captures the full cycle of spatial-temporal bubbly shock creation and subsequent evolution in the diverging section of the nozzle. We revealed a direct connection between the injected bubbles and the emitted bubbly shock waves traveling downstream. We show that the second harmonic frequency, as observed in the dynamical pressure data, can be attributed to the reflections of these decaying downstream shock waves from the previous cycle.

Our shock wave enhancement technique has some analogy to the synthetic schlieren method [38,39] where digital image processing is used to infer the variations of refraction index to variations of the media physical properties. In contrast, our enhanced gradient shadowgraphy technique is different from the working principles associated with standard schlieren visualization techniques [40]. A schlieren setup detects changes to the first derivative in density via translating phase speed differences in light into intensity change as light passes through a test section medium. In our case, the resulting colored images correspond to the strength of the change in a pixel intensity temporal gradient. Our study focuses on the physics associated with the intensity increase. Thus, in the results to be presented, we employ a hot colormap superimposed with recorded frames without the cool colormap.

In the Supplemental Material [41], two GIF files are used to illustrate the enhanced gradient-shadowgraphy technique application as described in Fig. 3. The first file (JP-5_pbp0_0.36_injL_G.gif) shows the first 200 animated raw frames (full nozzle view) in slow motion (10 frame/s) of aerated (single injector active) JP-5 flow at the nozzle's outlet-inlet pressure ratio $p_b/p_0 = 0.36$. The second file (JP-5_pbp0_0.36_injL_GHC.gif) shows these raw frames with hot and cool colormaps obtained from the enhanced gradient-shadowgraphy technique.

IV. RESULTS

In this section a detailed characterization of the bubbly shock wave creation mechanism in aviation fuel cavitation and a quantitative assessment of shock wave evolution in aerated cavitating flow are provided. Two commonly used aviation fuels are considered in our study, JP-5 and JP-8, at four nozzle outlet-inlet pressure ratios: $p_b/p_0 = 0.25, 0.36, 0.47, 0.58$, where p_b denotes the nozzle back pressure at $x/L = 1$ and p_0 is the nozzle inlet pressure at $x/L = 0$ (for aerated cases its values varied in range of $p_0 = 92 \pm 1$ kPa and for nonaerated cases in range $p_0 = 88 \pm 0.5$ kPa). At each of these pressure ratios, the flow is choked due to the effective compressibility of the two-phase flow. In this choked flow regime, the volumetric flow rate does not change with variation of back pressure as shown in Fig. 4. For each fuel the measured value was $Q = (3.34 \pm 0.037)\times 10^{-5}$ m^3/s, which is equivalent to a mass flow rate of 0.0264 kg/s for JP-5 and 0.0263 kg/s for JP-8 (using densities 808 kg/m^3 and 777 kg/m^3 for JP-5 and JP-8, respectively). It should be noted that for a pressure ratio of $p_b/p_0 > 0.58$, which is a nonchoked flow regime, there was no evidence of bubbly shock waves. In the choked flow regime, all back pressures in our study yielded a pressure drop that was large enough to cause unsteady bubbly shock waves to form and travel downstream in the diverging section of the nozzle.

We provide four definitions of the cavitation number as follows:

$$\sigma_0 := (p_0 - p_v)/\big(0.5\rho_f U_0^2\big), \tag{1a}$$

$$\sigma_{th} := (p_{th} - p_v)/\big(0.5\rho_f U_{th}^2\big), \tag{1b}$$

$$\sigma_{\min,0} := (p_{\min} - p_v)/\big(0.5\rho_f U_0^2\big), \tag{1c}$$

$$\sigma_{\min,th} := (p_{\min} - p_v)/\big(0.5\rho_f U_{th}^2\big). \tag{1d}$$

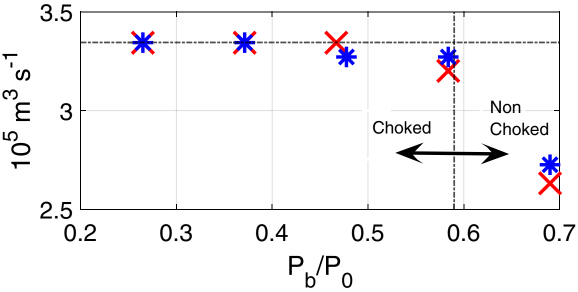

FIG. 4. Volume flow rates of aerated JP-5 (red X symbols) and aerated JP-8 (blue asterisk symbols) obtained with uncertainty of $e_Q = 3.7\times10^{-7}$ m^3/s. The horizontal dashed line denotes the value $Q = 3.34\times10^{-5}$ m^3/s.

Here p_v and ρ_f denote fluid vapor pressure and density at nominal conditions, respectively. The vapor pressures of JP-5 and JP-8 are close to $p_v = 0.24$ kPa (at room temperature) based on interpolated data from [31,32]. For the reference densities, we use 808 kg/m^3 and 777 kg/m^3 for JP-5 and JP-8, respectively. $U_0 = Q/A_0 = 1.1 \pm 0.01$ m/s and $U_{th} = Q/A_{th} = 13 \pm 0.14$ m/s are velocities obtained by using volumetric flow rate Q and the cross-section area A_0 at nozzle inlet ($x/L = 0$) and A_{th} at nozzle throat ($x/L = 0.2$–0.25), respectively. The corresponding throat Reynolds number is $\text{Re}_{th} = Q_{ch}/(\sqrt{A_{th}}\nu) = 1.3\times10^4$. The viscosity ν of JP-5 and JP-8 is in both cases taken to be 1.6×10^{-6} m^2/s at 20 °C [31,32]. p_0, p_{th} are the static pressures obtained by static sensors located at $x/L = 0$ and $x/L = 0.2308$, respectively; $p_{\min}$ is the minimum value of static pressure obtained along the center line of the nozzle profile (the values in $x/L = 0.2$–0.5 range as shown in Fig. 1). Both U_0 and p_0 were fixed for all pressure ratios in the choked flow regime. The resulting values are obtained with relative uncertainty of $e_\sigma/\sigma = 2\%$ and summarized in Table I for aerated and nonaerated JP-5. The cavitation number for JP-8 was about 4% higher for all cases (aerated and nonaerated). Table I shows that the cavitation number was positive in all cases.

Next, we discuss the two observed mechanisms of bubbly shock wave generation present in aerated and nonaerated cavitation cases. Then we focus on aerated cases, where the strongest shocks are observed, the behavior of which we quantify for different controlled parameters such pressure ratios and bubble injection rates.

A. Bubbly shock wave generation mechanisms in choked aerated and nonaerated cavitation cases

In Fig. 5 a typical, single full cycle of the bubbly shock wave generation mechanism for aerated cavitation is shown. In particular, the cycle is shown for JP-8 fuel at $p_b/p_0 = 0.25$ with single hole

TABLE I. Cavitation number summary using the definitions in Eqs. (1a)–(1d) for aerated and nonaerated JP-5 fluid. The cavitation number for JP-8 was about 4% higher for all cases (aerated and nonaerated). The data shown are obtained with cavitation number relative uncertainty up to $e_\sigma/\sigma = 2\%$.

JP-5	p_b/p_0	0.25	0.36	0.47	0.58
Aerated	σ_0	182.0	181.9	181.4	181.5
	σ_{th}	0.21	0.26	0.31	0.40
	$\sigma_{\min,0}$	4.05	11.48	23.96	45.19
	$\sigma_{\min,th}$	0.02	0.08	0.16	0.31
Nonaerated	σ_0	186.0	185.6	185.2	185.4
	σ_{th}	0.16	0.16	0.16	0.30
	$\sigma_{\min,0}$	3.92	6.84	10.80	34.73
	$\sigma_{\min,th}$	0.02	0.04	0.07	0.24

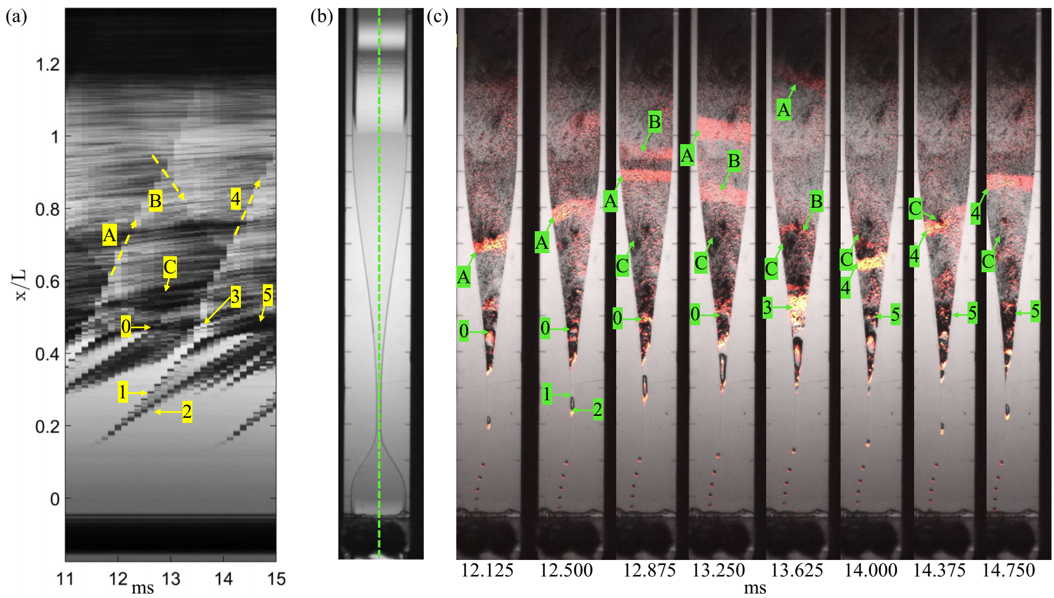

FIG. 5. A single full cycle of the bubbly shock wave generation mechanism for JP-8 at $p_b/p_0 = 0.25$ and single bubble injector. (a) Time history (11–15 ms) of full nozzle along its centerline which denoted in plot (b). (b) Empty nozzle as captured by camera with centerline denoted by green dashed line. (c) Representative hot colormap (from applying enhanced gradient shadowgraphy) superimposed with recorded frames, within the cycle, labeled by the time of capture. In plots (a) and (c), the corresponding events/structures are denoted by numbers and letters as follows: (0) attached cavity cloud; (1) oncoming bubble downstream (top) edge; (2) oncoming bubble upstream (bottom) edge; (3) collapse event; (4) emitted downstream propagating shock wave; (5) new cavity cloud; (A) emitted downstream propagating shock wave from previous cycle; (B) reflected upstream propagating shock wave from previous cycles; (C) detached cavity cloud from previous cycles.

microbubble injection. The injected train of bubbles enters the throat at a rate of 423 Hz (determined by counting bubbles passing through the throat per unit time. More details are provided in the following Sec. IV B). We present a single cycle as it is captured in the space-time history chart (from 11–15 ms) of the full nozzle shown in Fig. 5(a) along the nozzle centerline [Fig. 5(b)], with representative single frames employing enhanced gradient shadowgraphy shown in Fig. 5(c) in the same time range. Numbers and letters denote the corresponding events in the frames (labeled by their capture time) and time history chart. The plot reveals a direct connection between the injected bubble path with the emitted/reflected shocks. The cycle starts with the existing and sustained attached cavity cloud (denoted by 0 in the t-x/L diagram and image frame labeled by 12.125 ms), whose upstream (bottom) edge is shown at the inception cite, $x/L = 0.3$, and its downstream (top) edge ends at $x/L = 0.5$. A single bubble at a time enters the throat (starting at $x/L = 0.2$). During propagation, the bubble grows. This growth is evident in the t-x/L diagram [Fig. 5(a)], where we show the top edge (1) and bottom edge (2) traces (black inclined lines in the range $x/L = 0.2$–0.4) exhibit different slopes, with the top edge slope slightly steeper. As the bubble approaches the cavity cloud (0) bottom edge, the cloud starts to retreat upwards (downstream direction), and the cavity shrinks. Once its bottom edge reaches $x/L = 0.5$ it collapses (the bright white spot at $x/L = 0.4$ in the t-x/L diagram), and a shock wave (4) is emitted in the downstream (upwards) direction, which is manifested in the t-x/L chart as a white inclined line with positive slope (with respect to the time axis) starting from $t = 13.625$ ms and $x/L > 0.5$. Meanwhile, the bubble that triggered the cavity collapse gives rise to the formation of a new cavity cloud (5), whose inception begins from the bubble bottom edge, and the cycle is completed. In Waldrop and Thomas [35], it was shown via detailed time-resolved pressure measurements that the collapse event is characterized by pressure pulses of very short duration and large magnitude, and the upstream bound of the cloud collapse process is shown to coincide with the lowest pressure in the static pressure distribution. Whereas the downstream collapsing bound, where the bubbly shock is emitted, is shown to lie where the static pressure distribution first rises to a value near the nozzle back pressure (within 2% of inlet pressure).

Within the time cycle shown in Fig. 5(a), we capture a downstream propagating bubbly shock wave (A), an upstream propagating shock wave, traveling from the nozzle outlet towards the throat, and a detached cavity cloud (C) from the previous cycle. The upstream traveling shock waves are weaker than the downstream traveling shocks, as manifested by the lower hot color intensity in the frames of Fig. 5(c) and the gray lines with negative slopes (with respect to time axis) in the t-x/L chart in Fig. 5(a) (and also in Figs. 13 and 14 in Appendix B). We assume that these upstream traveling shocks are reflections of the decaying downstream shock waves from the previous cycle. The downstream shock is most intense at $x/L = 0.35$–0.5, near the collapse region close to the throat exit. Interestingly, a careful look at frames in Fig. 5(c) in the range 13.625–14.750 ms reveals that both downstream (A) and upstream (B) shock wave fronts are distorted when they encounter a cavity cloud (C) but restore their uniform planar wave-front right after passing it. We also observe that the shed cavity cloud shrinks in its size and experiences weaker collapse events. The decay of bubbly shock waves farther downstream was also quantified by dynamic pressure measurements in [35,37], where average pressure jumps of 36.6 kPa, 12.6 kPa, 9.5 kPa, and 8.8 kPa were documented at $x/L = 0.4$, 0.8, 0.9, and 1.0, respectively, for aerated dodecane at $p_b/p_0 = 0.36$, which demonstrates the reduction in pressure jump magnitude of a typical shock as it propagates downstream. Example plots of these shock pressure profiles in dodecane flow through a CD nozzle are provided in [35, Fig. 7].

In the Supplemental Material [41], two GIF files can be found that animate the entire process so as to further illustrate the findings from Fig. 5 for aerated (single injector active) JP-8 flow at $p_b/p_0 = 0.25$. The first file (JP-8_pbp0_0.25_injL_GH.gif) shows a full nozzle view (at resolution of $a = 0.1896$ mm/pixel). The second file (JP-8_pbp0_0.25_injL_GH_zoomed.gif) shows a zoomed-in view ($x/L = 0.2$–0.7) at higher resolution ($a = 0.0552$ mm/pixel). Both GIFs show the first 200 raw frames superimposed with a hot colormap obtained from the enhanced gradient-shadowgraphy technique, and animated in slow motion (10 frame/s). In addition, in Fig. 12 in Appendix A we provide a zoomed-in view ($x/L = 0.2$–0.7) of consecutive frames capturing the single full cycle of period bubbly shock wave generation mechanism for JP-8 at $p_b/p_0 = 0.36$ and single bubble injector.

In naturally occurring cavitation (nonaerated), the inception occurs on the nozzle sidewalls just downstream of the throat, beginning at $x/L = 0.3$. Figure 6 presents instantaneous images of natural cavitation in JP-8 for a range of nozzle pressure ratios. These images show that the cavitation inception location does not vary with changes in back pressure. Furthermore, for different experimental runs cavitation can initiate on either of the nozzle side walls with the resulting pattern being remarkably symmetric. In this flow regime, the cavity sheet is sustained and attached to the nozzle sidewall, while cavity clouds are shed in a swirling motion from its downstream (trailing) edge. The same behavior is observed for JP-5 as in JP-8. In this regime, static pressure measurements for the fully cavitating choked flow regime were reported in Dunn *et al.* [2] and Dorofeeva *et al.* [34] for JP-8 in the same nozzle geometry. The static pressure reaches a minimum value of $p/p_0 = 0.09$ at $x/L = 0.35$, which is shown in Fig. 1. Details regarding similar cavity structures resulting from natural cavitation in a venturi nozzle with water are reported in Tomov *et al.* [15].

The enhanced shadowgraphy technique was also applied to natural (nonaerated) fuel cavitation to examine the shock emission mechanism from shed swirling cavity clouds previously described. Figure 7 shows a frame by frame analysis of JP-8 at $p_b/p_0 = 0.25$ with 0.125 ms between each frame. This shows weak bubbly shock waves emitted from shed swirling cavity clouds in the nonaerated cavitation flow regime (without bubble injection). Small shocks are evident but much weaker in their intensity than in the aerated cases. The cloud's core is sustained due to low pressure

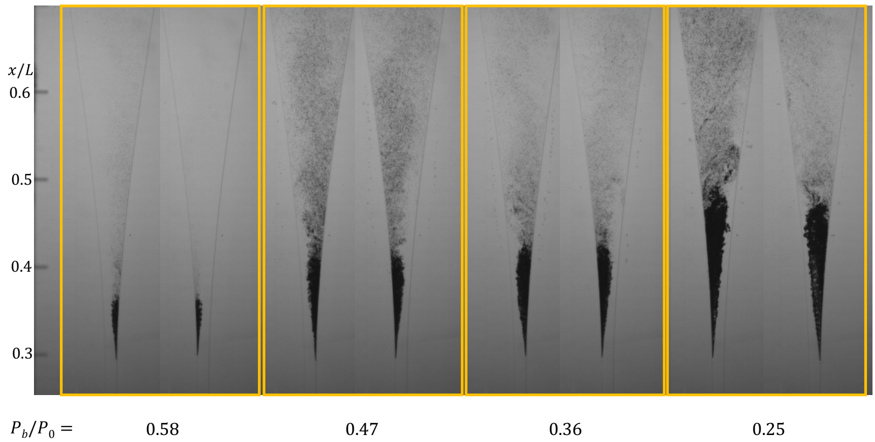

FIG. 6. Nonaerated cavitation inception. Instantaneous frames for JP-8 at different back pressures, for the nonaerated choked regime. For each pressure, two frames are shown capturing sheet-cavity inception at $x/L = 0.3$ for two possible scenarios: on the left and right side wall.

at the center of the induced vortical motion. As it moves downstream, the static pressure in the nozzle rises, triggering the cloud to collapse inwards from the cloud's external perimeter, which results in shock waves emitted in the direction tangential to the swirling cloud. After the collapse, the cloud starts to grow once again towards its original size (which is bounded by nozzle side walls), and the collapse process is then repeated. The inward collapse was also observed in past studies in water. For example, in [5], the shock wave strengthens considerably as it propagates into the cloud, primarily because of geometric focusing. One consequence of this is that the closer

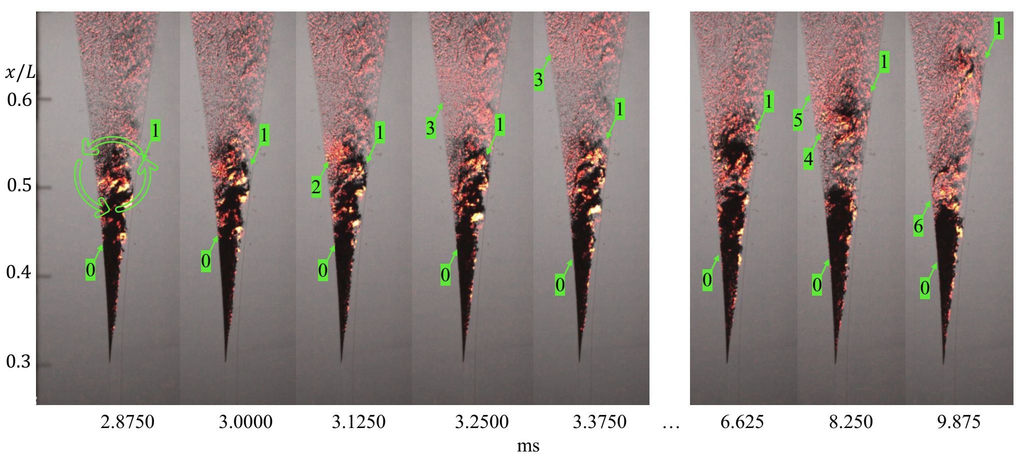

FIG. 7. Mechanism of bubbly shock wave creation due to shed cavity clouds in the nonaerated cavitation flow regime (no bubble injected) illustrated via snapshots of JP-8 at $p_b/p_0 = 0.25$ labeled by the time of capture. The corresponding events/structures denoted by numbers as follows: (0) attached stationary main cavity body; (1) detached cavity cloud at swirling motion; (2) collapse event at the detached cavity cloud; (3) emitted shock wave; (4) additional collapse event at the detached cavity cloud; (5) emitted shock wave in a tangential direction from the detached cavity cloud's external perimeter during its collapse inwards; (6) new collapse event at the detached cavity cloud.

the bubbles are to the cloud center, the smaller the size to which they collapse. Very complicated bubble-bubble interactions are observed, and very high pressures are generated when the focusing shock reaches the center of the cloud. Then, a spreading expansion wave causes all bubbles to grow and begins another cycle of cloud oscillation. In the Supplemental Material [41], a GIF file (JP-8_pbp0_0.25_GH_zoomed.gif) can be found that animates the process so as to further illustrate the findings from Fig. 7 for nonaerated JP-8 flow at $p_b/p_0 = 0.25$. This GIF shows the first 101 raw frames superimposed with a hot colormap obtained from the enhanced gradient-shadowgraphy technique and animated in slow motion (10 frame/s).

The strongest bubbly shock waves are emitted in the aerated flow cases due to the first mechanism triggered by injected bubbles described previously. The weaker shock wave mechanism is associated with the detached shed swirling cavities from the sheet-cavity main body. In the aerated flow, both mechanisms are observed.

B. Characterization of bubbly shock wave emission and propagation in aerated cavitation

This section is focused on further analysis of the aerated flow cases, where the most violent shock waves are emitted. In the aerated case, we can control the bubble injection rate (i.e., inlet void fraction) and nozzle pressure ratio to characterize the bubbly shock propagation with respect to these parameters.

In Fig. 8(a) we show the t-x/L diagram for the nozzle centerline but with a longer time duration of 125 ms for JP-8 at $p/p = 0.25$. A direct connection between the injected bubbles and the emitted bubbly shock waves in the aerated flow regime is evident. After each bubble trace (observed over the range $x/L = 0.2$–0.25) there is a downstream propagating shock wave trace (at range $x/L = 0.6$–1). In addition, in the diverging section range $x/L = 0.6$–1, dark inclined regions are evident and represent convected cavity clouds detached from the attached cavitation region at $x/L = 0.5$. The dark shed-cavity-cloud-regions' appearance frequency, and their slopes reveal that the detached cavities are shed after each bubble passing through the throat. Then this cloud region merges with previously shed cavities near $x/L = 0.6$. The frequency of the merged cloud group varied in the range $f_c = 80$–140 Hz (the frequency increased with back pressure increase) and was not synchronized with the emitted bubbly shock waves. The corresponding Strouhal number varied in the range $\mathrm{St} = f_c l_c/v_{th} = 0.033$–$0.057$, where $v_{th} = 13$ m/s, is the flow velocity at the throat, which was constant in the choked flow regime for both fluids for all pressures and injection setups; $l_c = 0.042L$ (0.0053 m) is the characteristic cloud length. We define l_c to be equal to the nozzle width at $x/L = 0.5$, where the detachment typically occurs for lower back pressure. For higher back pressure, it occurred earlier at $x/L = 0.4$, and the shed cloud characteristic length, l_c, was shorter and corresponded to the nozzle width at $x/L = 0.4$. The obtained Strouhal numbers are lower than values reported in similar nozzle flow settings with water, such as [15], which is not surprising since we obtain it for the merged clouds. A more detailed study of the dynamics of the reentrant jet and the cavity shedding mechanisms with fuels are beyond the scope of this paper and is a topic for future study. From the shed merged cloud slopes in the time-space diagram, we determine the convected speed is approximately 3 m/s, much lower than the emitted shocks speed [20–80 m/s, with much steeper slopes, which appear as bright nearly vertical lines in Fig. 8(a)]. Although each shed cavity and collapse event is triggered by the oncoming bubble exiting from the throat, the two bubbly shock wave emission mechanisms seem to be independent of the cavity-clouds-merging events at the diverging section's latter stages. The synchronization is more evident between the collapse events and shed cavities with back pressure increase, as illustrated in centerline time history plots of JP-5 and JP-8 in Appendix B (Figs. 13 and 14, respectively).

To further quantify the propagation of the dominant bubbly shocks concerning different flow parameters, the t-x/L chart in Fig. 8(a) is binarized, and filtering is applied to isolate the traces of entering bubbles to the throat, and the traces of downstream traveling bubbly shocks. The weaker bubbly shock waves, which are emitted due to shed cavities from the downstream (trailing) edge of

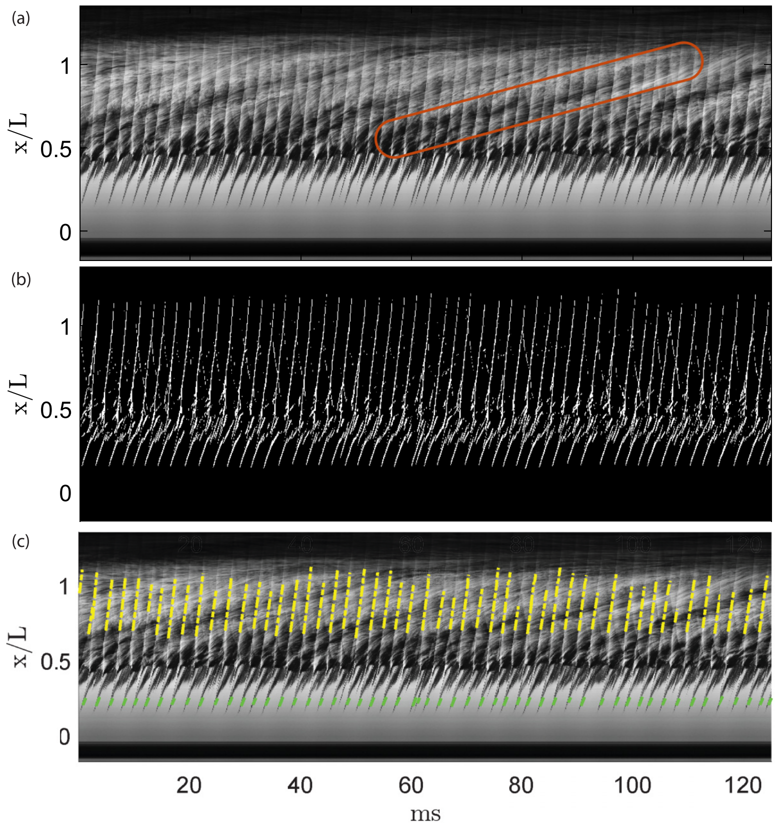

FIG. 8. (a) Typical centerline time history (shown for JP-8 $p_b/p_0 = 0.25$, and single injector). One of the convected cavity clouds is highlighted by the brown oval. (b) Binarized filtered map with extracted bubble and upwards traveling shock wave traces. (c) Fitted curves to bubble bottom edge traces (green) and downstream traveling shock wave traces (yellow).

the attached sheet cavity, and those that are reflected and travel upstream are removed during this processing. In Fig. 8(b) we show the resulting map.

A systematic quantitative analysis is performed to gain insights on the impact of pressure ratio and the void fraction on the downstream shock waves' propagation speed in the aerated flow cases, where the most violent bubbly shock waves are emitted. To do so, the segmented binary images, connected components (line curves) are extracted, and linear curves are fitted to find the lines' slopes at different heights. The fitted curves are shown in Fig. 8(c). In the throat region, $x/L = 0.2$–0.25, curves were fitted to the bubble bottom edge traces, and in the range $x/L = 0.6$–1 for downstream traveling shock wave traces. The average slope values of the curves for the $x/L = 0.2$–0.25 and $x/L = 0.6$–1 ranges are used to obtain the detected bubble velocity and shock wave velocity, respectively. Also, the bubble lengths are measured and their traces are counted to determine the bubbles passage frequency through the throat. These bubble metrics are used to obtain the void fraction as well, as will be detailed next. The analysis is applied to both aerated JP-5 and JP-8 fuels at four back pressures, $p_b/p_0 = 0.25, 0.36, 0.47, 0.58$, all within the choked flow regime, and with two bubble injection setups (with one or two injector openings) as demonstrated in Fig. 9(a). These experimental conditions are summarized in Table II.

First, in Fig. 9(b) we show the bubble terminal velocity in the $x/L = 0.2$–0.25 range. The bubble velocity is observed to be fairly constant (varies between 10.4 and 11.8 m/s) for all frequencies and

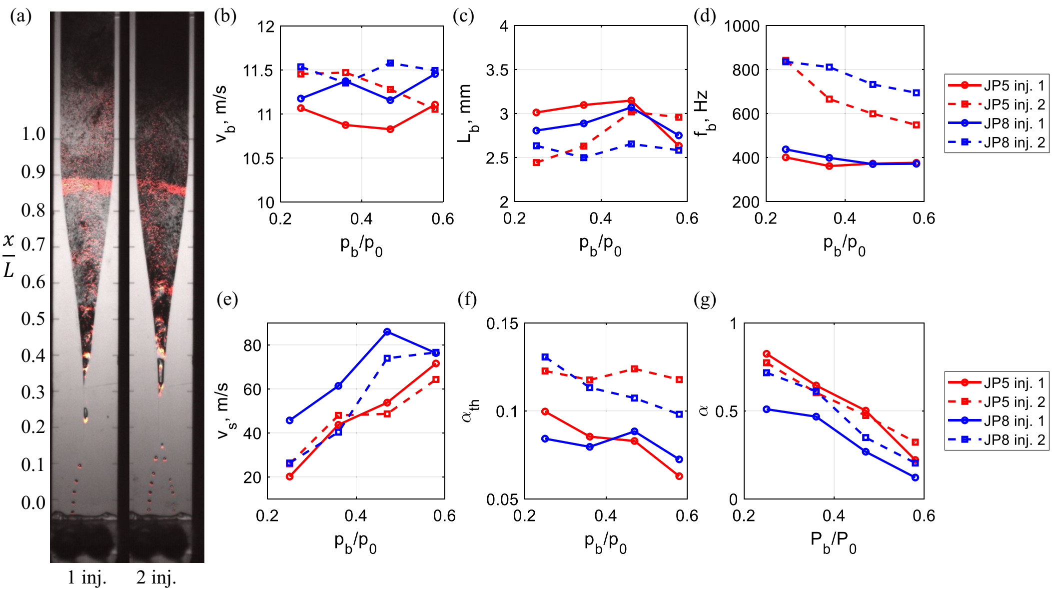

FIG. 9. (a) Snapshot for two bubble injection setups (left: single injector, right: two injectors. Shown for JP-8 and $p_b/p_0 = 0.25$). (b) Bubble terminal velocity, v_b, at the throat ($x/L = 0.2$–0.25) obtained with uncertainty up to 7.9%. (c) Bubble average length, l_b, at the throat obtained with uncertainty up to 7.6%. (d) Bubble passage frequency, f_b, through the nozzle throat (sampled at $x/L = 0.22$ obtained with uncertainty up to 3.4%). (e) Downstream (upwards) traveling shock wave speed, v_s, in range $x/L = 0.6$–1 obtained with uncertainty up to 4%. (f) Throat void fraction, α_{th} (at $x/L = 0.2$–0.25), obtained with uncertainty up to 15%. (g) Outlet void fraction, α, at the diverging part of the nozzle ($x/L = 0.25$–0.1) obtained with uncertainty up to 10%.

injector setups for both fuels. This is not surprising as in choked flow, decreasing the back pressure does not impact the mass flow rate through the nozzle throat.

Second, by detecting the bubble top and bottom edges, we can also measure each bubble's length along the centerline during passage through the throat. In Fig. 9(c) we show the average length, which varies in the range 2.5–3.5 mm ($0.0197L$–$0.0276L$) for all frequencies and injector setups for both fuels, and this seems to be invariant with back pressure variations in the choked flow regime. These values will be used for computing void fractions in the throat as described later in this section.

Third, we show in Fig. 9(d) the bubble passage frequency, f_b, through the nozzle throat (at $x/L = 0.22$), which we could determine to an uncertainty of within 3.4% (by multiple runs, over at least five runs of the code over different video segments of each case and duration). Because the flow rate is constant at choked flow, the bubbles entering the nozzle travel at a constant velocity and have similar sizes, which does not change with back pressure [as shown in Figs. 9(b) and 9(c), respectively]. We suggest that the frequency increase for two injectors is related to the distance between the bubbles, which decreases with the addition of a second injector and as back pressure decreases. Adding a second injecting hole increases the bubble passage frequency approximately

TABLE II. Summary of experimental conditions for the aerated case.

Fuel types	Pressure ratios p_b/p_0	Active injectors
JP-5, JP-8	0.25, 0.36, 0.47, 0.58 (choked flow)	Aerated: 1,2

by 200% but not uniformly for different back pressures. We explain this by observing from the video frames that the second injector injected smaller bubbles at a slightly lower rate than the first injector. Interestingly, for all cases, the frequency decreases with increasing pressure ratio in the range 0.25–0.58 by approximately 15%, aside from the case for JP-5 with two injectors where it was about 30%—we conjecture that it is due to a second injector performance issue for those particular four experiments with JP-5. As for the single injector, the decrease was consistent with the JP-8 data. Despite the choked flow, it is still very likely, particularly in a real experimental environment, that back pressures that approach the choking threshold ($p_b/p_0 = 0.58$) would impact the nozzle inlet conditions and thus affect the bubble release from the injectors. The reduction in the nozzle's back pressure close to the choking threshold may increase instantaneous subatmospheric pressure fluctuations in the nozzle inlet section (which will not be evident in time mean pressure and flow rate measurements), increasing the injection rate slightly from the syringe in the medical pump. This can be supported by the observation reported in [42] which showed that bubble distribution increases the probability of inception owing to the migration of the bubbles to the low-pressure regions. In addition, the authors of [33] monitored a single macro bubblegrowth over a 1-mm-deep hole under different subatmospheric conditions for aviation fuel (JP-8), dodecane, and distilled water. They noted that the bubble detachment from the nucleation site was very sensitive to pressure variation. In the Supplemental Material [41], two GIF files can be found that animate the process so as to further illustrate the findings from Fig. 9(d) for aerated JP-8 flow at $p_b/p_0 = 0.25$. The first file (JP-8_pbp0_0.25_injL_GH.gif) shows a full nozzle view with the single injector active. The second file (JP-8_pbp0_0.25_inj2_GH.gif) shows a full nozzle view with two bubble-train injectors active. These GIFs show the first 200 raw frames superimposed with a hot colormap obtained from the enhanced gradient-shadowgraphy technique and animated in slow motion (10 frame/s). The choking at the throat leads to a constant flow rate. Thus, the injected bubbles at the nozzle inlet propagate towards the throat and pass through it at the same velocity, where only one bubble passes at a time. By introducing an additional injector, we increase the bubble injection rate, which leads to reduced distances between them at the inlet section before they enter the throat. Therefore, it still will pass the throat at the same velocity but at a higher frequency.

Fourth, in Fig. 9(e) we demonstrate that for both aviation fuels and injector setups, the shock wave speeds monotonically increase from 25 m/s for the lowest back pressure to 80 m/s for the highest back pressure in our study. The relative uncertainty of the bubble length l_b, bubble velocity in the throat v_b, and shock speeds in the diverging section v_s are found to be, $e_{l_b}/l_b = 7.6\%$, $e_{v_b}/v_b = 7.9\%$, and $e_{v_s}/v_s = 4\%$, respectively, which were obtained using resolution $a = 0.1896$. Here e_{v_b}/v_b and e_{v_s}/v_s are obtained from the observed slopes $(r/\delta t)$ in x-t diagrams [see the example in Fig. 8(c)], using the expression $e_v/v = e_r/r$ (based on the fact that displacement is a dominant factor that contributes to velocity uncertainty), where e_r is an error of an average displacement r.

In the literature, the shock wave speed is considered with respect to the void fraction parameter. Void fraction is a key quantity of interest in studies of cavitating flow. Here the void fraction definition is

$$\alpha := \frac{V_g}{V_g + V_l}, \tag{2}$$

where V_g is gas/vapor phase volume and V_l is liquid phase volume. In Figs. 9(f) and 9(g), we show the evaluated mean void fractions in the nozzle throat ($x/L = 0.2 - 0.25$), α_{th}, and in the diverging section ($x/L = 0.25$–1), α. Details of how we compute the void fraction in the diverging section are presented in Appendix C. For both JP-5 and JP-8, similar values of $\alpha_{th} \approx 0.1$ are obtained and remain fairly constant with pressure variation. α_{th} is slightly higher (increased by $\approx$0.025) when a second injector hole is added. The similarity in α_{th} between the two fuels may be due to their similar air solubility, which for JP-5 and JP-8 is 0.15 and 0.16 mm^3 of gas/mm^3 of fuel at 20 °C, respectively. The void fraction in the throat is considerably higher than in the inlet, α_0 which was obtained in similar manner. In the nozzle inlet, the syringe injection frequency was 1200 Hz, and the measured average bubble diameter exiting the needle is 0.74 mm for all pressures and both liquids.

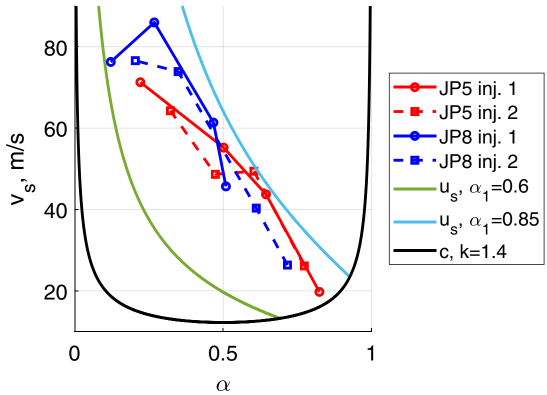

FIG. 10. Shock speed, v_s, as a function of average void fraction in the diverging section ($x/L = 0.25$–1), α. Also shown are upstream shock speeds, u_1, governed by Eq. (3), for two upstream void factions α_1 and sonic velocity obtained from Eq. (5), for $\frac{p_1-p_v}{\rho_L} = 25\ \mathrm{m^2/s^2}$ and $\frac{2S}{\rho_L R_1} = 0.1\ \mathrm{m^2/s^2}$ and $k = 1.4$.

This yields $\alpha_0 = 0.007$ and $\alpha_0 = 0.012$ for single and double injector setups, respectively. For more details on the injector performance and inlet void fraction assessment, see [35]. In the diverging section, the void fraction increases even more significantly. In Fig. 9(g), we show the evaluated mean void fraction in the diverging section of the nozzle, α, in the region ($x/L = 0.25$–1). For both JP-5 and JP-8, similar values α are obtained and these monotonically decrease from 0.8 to 0.3 with increase in back pressure. No significant differences are evident between the cases. Interestingly, there is little effect when a second injector is added.

In Fig. 10 the downstream propagating shock wave speed is plotted as a function of the obtained mean void fraction in the diverging section. The downstream propagating bubbly shock wave speed decreases with an increase in the obtained mean void fraction. In addition, we plot the upstream shock speed, u_1, and sonic velocity of the mixture, c_1, governed by the fully nonlinear solutions of the governing equations, where the dynamics of individual bubbles as manifest by the Rayleigh-Plesset equation is incorporated into the solutions, using the equations for nonbarotropic homogeneous flow, following the Brennen [6] formulation. In particular, the upstream shock speed, u_1, is obtained using

$$u_1^2 = \frac{1-\alpha_2}{(1-\alpha_1)(\alpha_1-\alpha_2)}\left\{\frac{p_1-p_v}{\rho_L}\left[\left(\frac{R_1}{R_2}\right)^{3k}-1\right]+\frac{2S}{\rho_L R_1}\left[\left(\frac{R_1}{R_2}\right)^{3k}-\frac{R_1}{R_2}\right]\right\}, \tag{3}$$

where α_2 is the void fraction far downstream of the shock and the bubble radius ratio, $\frac{R_1}{R_2}$, before and after shock is

$$\left(\frac{R_1}{R_2}\right)^{-3} = \frac{\alpha_2(1-\alpha_1)}{\alpha_1(1-\alpha_2)}. \tag{4}$$

Here upstream and downstream shock wave conditions are denoted by subscripts 1 and 2, respectively. This assumes the existence of an equilibrium state far downstream of the shock. Also displayed in this figure is the sonic velocity of the mixture, c_1, under the upstream conditions given by

$$c_1^2 = \frac{1}{\alpha_1(1-\alpha_1)}\left[\frac{k(p_1-p_v)}{\rho_L}+\left(k-\frac{1}{3}\right)\frac{2S}{\rho_L R_1}\right]. \tag{5}$$

Since fuel is a multicomponent hydrocarbon, there is some uncertainty in assessing exactly the liquid properties of JP-5 and JP-8 fuels, such as vapor pressure p_v, and surface tension S. However, one can still solve Eqs. (3)–(5) by estimating that $(p_1 - p_v)/\rho_L = 25\ \mathrm{m^2/s^2}$, where for the upstream

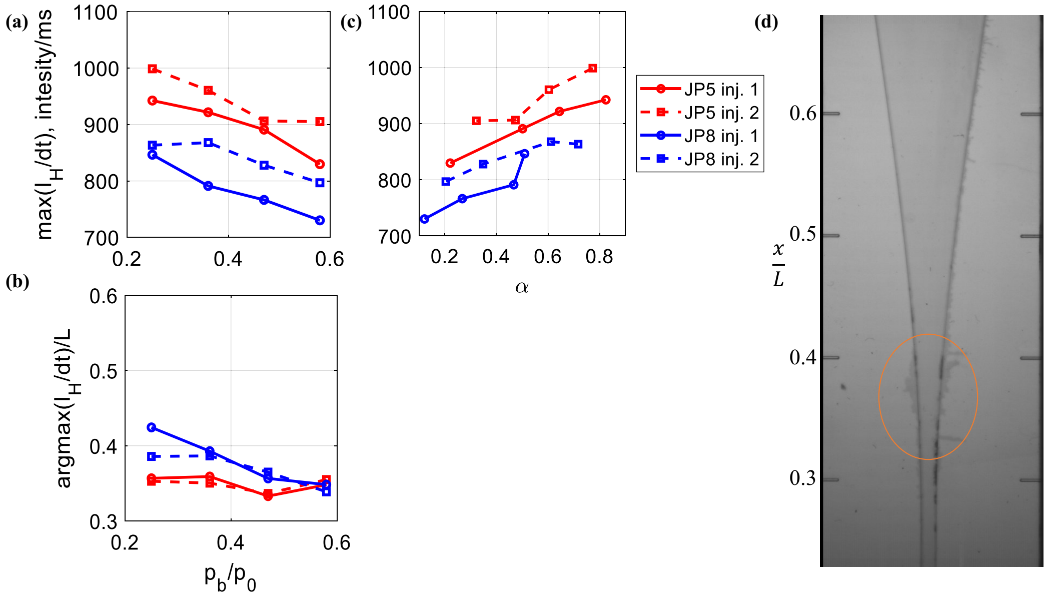

FIG. 11. Gas-to-liquid phase change rates to characterize the magnitude of the cavity collapse events and shock-wave emission intensity. (a) The magnitude of intensity increase gradient, $\langle \max_{x/L}(I_H/dt)\rangle_t$, which is a maximal value of $I_H/\Delta t$ along the nozzle centerline, extracted for each frame and then averaged over 1000 frames. (b) $\langle \arg\max_{x/L}(I_H/dt)\rangle_t$, location where maximum of intensity gradient occurs. (c) $\langle \arg\max_{x/L}(I_H/dt)\rangle_t$ as function of average void fraction in the diverging section. (d) Zoomed-in view on the CD nozzle's diverging section to show the erosion damage (highlighted by the orange oval) after performing multiple aerated experimental runs.

pressure p_1 of the shock wave, we assume the lowest nozzle back pressure in our study, which is $0.2p_0 = 20$ kPa; the vapor pressures of JP-5 and JP-8 are below $0.1p_0$ [31,32], and thus not significant for the gaseous cavitation considered here, and the density is taken to be 800 kg/m^3, which is fairly close to the JP-5 and JP-8 densities, which are 808 kg/m^3 and 777 kg/m^3, respectively. We also assume isentropic ($k = 1.4$) bubble/cavity behavior. The surface tension, S, of JP-5 and JP-8 is 23.8 and 23.2 mN/m at 20 °C, respectively [31,32], which is far below the surface tension of water which is 72.8 mN/m at 20 °C. Thus, we set $2S/(\rho_L R_1) = 0.1$ m^2/s^2 (as in [6] for bubbly flows in water), without explicitly defining R_1. It is found that the solution varies by only 3% with increase or decrease of that value over four orders of magnitude in the range (0.001–10 m^2/s^2).

Figure 10 shows a substantial similarity between our experimental data for aerated JP-5 and JP-8, and nonlinear solutions of the governing equations that are obtained and bounded between shock speeds, u_1, from nonlinear solutions for α_1 in the range $\alpha_1 = 0.6$–0.85. One can also see that propagating bubbly shock wave speed is bounded from below within the obtained range of sonic speed c_1, similar to reported studies in bubbly water flows [6].

Finally, the strength of the cavity cloud collapse is quantified, leading to bubbly shock wave emission events for the studied flow cases. We extract from hot colormaps obtained by the enhanced gradient shadowgraphy method the magnitude of the intensity increase gradient, $I_H/\Delta t$ (I_H is a positive change in intensity between two consecutive raw frames obtained over a Δt time difference), along the nozzle centerline for each frame. The typical hot map is shown in Fig. 3(b). We extract the maximal value of $I_H/\Delta t$ along the centerline [$\max_{x/L}(I_H/dt)$] and its location of occurrence [$\arg\max_{x/L}(I_H/dt)$]. Figures 11(a)–11(c) show an average of these values taken for over 1000 frames (over 125 ms duration).

Figures 11(a) and 11(c) reveal that $I_H/\Delta t$ increases with decreased back pressure and mean void fraction, α, increase. It is also evident that an increase in the bubble injection rate by adding a second injector hole increases slightly the magnitude of $I_H/\Delta t$. We associate the increase in $I_H/\Delta t$ to more violent collapse events and stronger bubbly shock wave emissions, which are observed for lower back pressures and bubble injection rates. Interestingly, these events are more violent for JP-5 than JP-8. The location where these events are most dominant is shown in Fig. 11(b). For all cases, this region varies within $x/L = 0.35$–0.42 when p_b/p_0 increased in the range 0.2–0.6 for JP-8, and fairly constant around $x/L = 0.35$ for JP-5. This coincides with static pressure profiles, which drop below $0.1p_0$ for the choked flow cases as shown in Fig. 1. Our results also agree with unsteady dynamic pressure sensor signatures of a typical shock presented in [35] for the same nozzle setup and flow conditions. The magnitude of the pressure jump across the shock decreases as it propagates downstream from the nearest sensor to $x/L = 0.35$. We observed cavitation erosion damage on the nozzle sidewalls [Fig. 11(d)] in the same region after performing multiple aerated experimental runs in a choked flow regime. In our experiments, the nozzle mold is covered by a top plate, which is firmly seated against the nozzle mold. In between, we place vacuum paste to close all possible gaps. However, after a few experimental runs with continuous bubble injection trains, over a 5–10 minute period, the bubble collapse on the side walls eroded the vacuum paste sealing and needed to be replaced each time after it happened.

V. CONCLUDING REMARKS

Bubbly shock wave propagation and generation processes in aviation fuel cavitation are experimentally characterized in a CD nozzle geometry. In past studies [2,34,35], considerable differences in cavitation in water and JP-8 aviation fuels are observed. A standing bubbly shock wave was observed in the water. However, it was absent in aviation fuels. A focus of the current study was to clarify the unsteady processes involved in fuel cavitation. Two fuels, JP-5 and JP-8, and two different flow regimes were studied: (1) aerated cavitating flow, where air microbubbles are injected at the nozzle inlet, and (2) nonaerated cavitating flow, where the flow evolved into the two-phase cavitating flow without bubble injection. For both fuels, the lowest local time mean static pressure was above the liquid-vapor pressure, supporting the gaseous cavitation scenario rather than vaporous cavitation. This is a major issue in fuel cavitation due to the high gas solubility of both JP-8 and JP-5. For both fuels, traveling unsteady bubbly shock waves are observed for all studied back pressures in the choked flow regime. In Preston *et al.* [36], different flow regimes are shown to exist in water cavitation depending on the value of the back pressure. They determined a critical back pressure after choking from which unsteady bubbly shocks appear and begin to travel downstream in the diverging section of the nozzle. In their simulation, this back pressure was determined by obtaining an accurate estimate of the critical radius of the bubbles for water. The authors noted that this unsteady bubbly shock wave is the correct solution in the regime where steady-state computations result in flashing solutions. In our study, the unsteady bubbly shocks were observed immediately after choking for both fuels and also for dodecane [35], and this may suggest that fuel cavitation does not have a steady standing shock flow regime as obtained in our previous experiments with water [2,34]. To accurately determine the unsteadiness thresholds in liquid fuels, designated experiments with better camera resolution and refined back-pressures close to choked flow thresholds should be carried out, focusing on the characterization of the bubble diameters in choked and nonchoked CD nozzle fuel flows. This is a worthy subject for future investigations.

A high-speed digital imaging shadowgraphy and shock-wave enhancement technique denoted as enhanced gradient shadowgraphy is developed and employed. This technique provided unprecedented details and quantitative information on the space-time evolution of bubbly shock waves and their interaction with cavity structures, which was only indirectly captured by pressure sensor data in the past experimental studies.

Two independent and sustained bubbly shock wave generation regimes are characterized, and plausible mechanisms are discussed. The first mechanism exists only in the choked aerated case (with bubble injection). In a single cycle of the mechanism, the triggered chain of events from the injected bubble entering the throat to bubbly shock wave emission takes about 2 ms. As the bubble approaches the existing and sustained attached cavity-cloud-upstream (leading) edge at the beginning of the diverging nozzle section where the static pressure drops below $0.1p_0$, the cloud starts to retreat downstream. Once its upstream edge reaches $x/L = 0.5$, it undergoes a sudden collapse, and a bubbly shock wave is emitted and propagates downstream. Meanwhile, the bubble that triggered the cavity collapse gives rise to the inception of a new cavity cloud at $x/L = 0.3$, and the cycle is completed. The emitted bubbly shock wave was intense enough to propagate through the entire passage and reflected upstream from the nozzle exit towards the nozzle throat before decaying completely.

The second mechanism exists in both aerated and nonaerated choked cases. This mechanism is isolated from the first mechanism by examining the nonaerated cavitation flow regime. In that mechanism, bubbly shock waves are emitted from the shed swirling cavity clouds, detached from the downstream (trailing) edge of the main body cavitating sheet region, whose inception is initiated at the nozzle sidewalls. When the swirling cloud propagated downstream, the back pressure increase triggers the cloud to collapse inwards from the edges (as the pressure in the cloud vortical core is sustained high). It results in bubbly shock waves emitted in the tangential direction of the swirling cloud. The study of the dynamics of the reentrant jet and the cavity shedding mechanisms without aeration is beyond this paper's scope and is a topic for future studies. Future studies will focus on further exploration of the cavitation inception mechanisms in these liquids, where more detailed unsteady pressure measurements are needed to confirm the gaseous cavitation scenario as assumed in our previous works [2,37], where the minimal local time-mean static pressure was near but above the liquid-vapor pressures. However, it is plausible that the pressure can go below the liquid-vapor pressure inside the vortical cores of the shed cavities, leading to both gaseous and vaporous cavitation.

In aerated cases, both proposed mechanisms coexist, where the first resulted in more violent collapse events and stronger shock waves than in the second. Interaction of bubbly shock waves from the leading-edge (first) mechanism is observed with the shed vortices from the trailing-edge (second) mechanism. Interestingly, both downstream and upstream shock wave fronts were distorted when they encountered a cavity cloud but restored right after passing it. The cavity cloud, in turn, shrinks in its size, and collapse events at the detached cavity cloud are observed.

A detailed quantitative analysis is performed to gain insights into the impact of the injected bubbles, the back pressure, and the void fraction on the downstream shock waves' speed and strength by employing time-history analysis along the nozzle centerline. Though the inlet's incoming bubble was accelerated and expanded, the measured bubble terminal velocity and length in the throat for choked flow is found to be reasonably constant and invariant with back pressure variations. Interestingly, the bubble passage frequency through the throat decreases with increasing back pressure. We suggest that the frequency increase should be related to the distances between the bubbles, decreasing with back pressure. Though the syringe injection rate was set to be constant and at a higher rate than imposed by the test-section vacuum conditions, we assume that the vacuum-driven-blowdown setup increases the bubble injection rate in the nozzle outlet with back pressure decrease, despite the choked flow regime.

The measured mean void fractions in the nozzle throat, for both JP-5 and JP-8 give similar values of $\alpha_{th} = 0.1$ and remain relatively constant with pressure variation. It is slightly higher (increased by 0.025) when a second injector is added. This value is one order of magnitude higher than the inlet void fractions [$\alpha_0 \sim O(0.01)$]. The mean void fraction in the diverging section monotonically increases with back pressure decrease and is significantly higher than in the void fraction in the throat. Similar behavior is observed in both fuels. Interestingly, although adding a second injector increases the void fraction in the throat, its impact in the diverging section is not significantly different as compared to cases with the single injector. We suggest it is possible that the cavities present in the nozzle's diverging section serve as a dominant nucleation site for creating the new cavities compared to the added bubbles from the second injector.

The bubbly shock waves speed increases from 25 to 80 m/s, with back pressure increase, and with the mean void fraction decrease. A strong similarity between our experimental data and nonlinear solutions of the governing equations is demonstrated. It adds further support to the grayscale method that we use to obtain the void fraction in the diverging section and may indicate that the mean void fraction can be incorporated in future modeling, simplifying the nonlinear equations that rely on upstream and downstream shock flow parameters, which may be challenging to obtain in practice.

More violent collapse events and stronger shock wave emissions were observed for lower nozzle back pressures and higher mean void fractions in the nozzle's diverging section, and increased bubble injection rates. Interestingly, these events are more violent for JP-5 than JP-8, despite the similarities (almost the same values) in their solubility, viscosity, surface tension, vapor pressure, and density. Determining the differences in fuel properties that cause it is subject to future studies but may well be due to different storage histories in the fuel samples used. The location where these collapse events are most dominant varies within $x/L = 0.35$–0.42 for JP-8, and is reasonably constant around $x/L = 0.35$ for JP-5, which coincides with static pressure profiles dropping below $0.1p_0$ and previously measured dynamic pressure signatures of the shock. In our experiments, we observed that in the same region of the nozzle erosion damage starts to appear after performing multiple aerated experimental runs at a choked flow regime.

Our enhanced gradient shadowgraphy image processing technique allows us to extract information that is typically challenging to obtain by shadowgraphy only. It enabled us to enhance phase changes and shock wave propagation and get quantitative data from nonintrusive imaging techniques usually employed for only qualitative assessment. This approach provides an avenue to explore cavitation and shock waves and should be used in future studies for different flow geometries. Still, as is the case in any experiment, there are inherent limitations, and complementary modeling and simulation efforts should also be applied in order to further address the detailed mechanisms of the bubbly shock generation characterized in this study. Results from our research shed some light on the complex physics of fuel cavitation. They may lead to improved fuel system components, which suffer from system performance degradation due to the damaging impact of the documented phenomena.

ACKNOWLEDGMENTS

The reported work was funded by the Honeywell International Corporation and the Office of Naval Research under Contract No. N00014-20-C-1010. This support is gratefully acknowledged. The experimental setup utilized for the research was initially developed as part of the Ph.D. dissertation research of Dr. Michael T. Waldrop, who kindly provided guidance on its use. We especially thank Abigail Parsons and Scott Rowan from Honeywell and Dr. Steve Martens of ONR for the many technical discussions during the course of this work.

APPENDIX A: BUBBLY SHOCK WAVE GENERATION MECHANISM IN AERATED FUEL FLOW

To further illustrate the findings from Fig. 5, in Fig. 12 we show a zoomed-in view ($x/L = 0.2$–0.7) at higher resolution ($a = 0.0552$ mm/pixel) of a typical, single full cycle of the bubbly shock wave generation mechanism for aerated cavitation. In particular, Fig. 12 shows consecutive frames of JP-8 fuel at $p_b/p_0 = 0.36$ with single injector active. The sequence of frames captures the following events/structures (denoted by numbers in each frame). The cycle starts with the attached cavity cloud (denoted by 0) that starts to shrink due to the oncoming injected bubble (1). We also denote the attached cavity inception site (2) is evident at the $x/L = 0.3$ region, as shown in the first frames (labeled by times in the range 14.625–15.125 ms). The cavity collapse (3) is observed in the image frame labeled by 15.375 ms, at $x/L = 0.44$ when the bubble front is at $x/L = 0.38$ (before the oncoming bubble touches it). Right after the collapse event, a bubbly shock (4), which is clearly

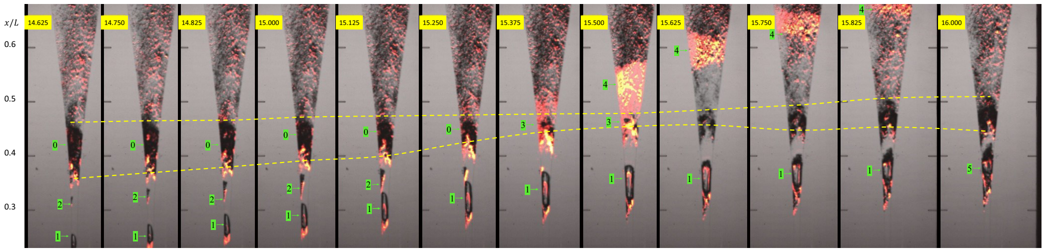

FIG. 12. A single full cycle of the periodic bubbly shock wave generation mechanism for JP-8 at $p_b/p_0 = 0.36$ and single bubble injector. Representative hot colormap (from applying enhanced gradient shadowgraphy) superimposed with recorded frames, within the cycle, labeled by the time (ms) of capture in the yellow rectangle on the top left corner of each frame. The corresponding events/structures are denoted as follows: (0) attached cavity cloud, with leading and trailing edges in each frames are marked by two yellow curves, bottom and top, respectively; (1) oncoming bubble approaching the cavity cloud and starts to shrink it; (2) natural inception site on nozzle side wall; (3) collapse event; (4) emitted downstream propagating shock wave; (5) new cavity cloud is incepted.

evident in the frame labeled by 15.5 ms, is emitted and propagates downstream. In the last stage of the cycle, the collapsed cavity expand, and the bubble that triggered the cavity collapse leads to the inception of a newly attached cavity (5).

APPENDIX B: OBSERVED SHED CAVITIES VIA TIME HISTORY CHARTS ALONG NOZZLE CENTER LINE

Space-time history charts are shown along the nozzle centerline of 125 ms duration for aerated JP-5 (Fig. 13) and aerated JP-8 (Fig. 14) at choked flow regime for outlet-inlet pressure ratios $p_b/p_0 = 0.25, 0.36, 0.47, 0.58$, and for single and double bubble injector setups.

APPENDIX C: VOID FRACTION CALCULATION

We are interested in assessing α in the diverging nozzle section where the bubbly shock waves exist and to study the impact of α on the shock wave speed in the aerated choked regime. To obtain α, we first evaluate the void fraction in the throat, α_{th}, by tracking the bubble average volume, $V_{b,th}$, and the bubble's passage frequency, f_b in the throat via the following relation:

$$\alpha_{th} = \frac{V_{b,th} f_b}{Q_{ch}}. \tag{C1}$$

Here $V_{b,th} = L_b A_{th}$, where we assume that the bubble occupies the entire cross section area, $A_{th} = (0.0126L \times 0.0126L)$, of the throat. The assumption is valid for voids larger than 1.6 mm (nozzle depth) in the nozzle section, which holds in our study, as shown in Fig. 9(c). More details on this assumption are provided in [43]. Q_{ch} is the volumetric flow rate in the choked flow regime, which is approximately $(3.34 \pm 0.037) \times 10^{-5}$ m^3 for all back pressures and for both JP-5 and JP-8.

The mean void fraction in the diverging section of the nozzle is obtained via the pixel intensity values as done in [2]. It is not a trivial task to obtain the void fraction from bubble shades due to the bright intensity of gas and liquid phase voids. The dark regions are due to the shadows from the created cavity boundaries and may not always reflect the correct amount of gas in large bubbles, with bright areas inside. Such grayscale intensity-based techniques have been employed to determine void fractions, where the flow characteristics are often assumed to be two-dimensional [44–46] and found to be reasonably reliable for obtaining void fractions with a swarm of tiny bubbles as compared to the x-ray imaging technique [47]. In our aerated cases, both conditions are satisfied in the diverging section, where nozzle depth, $0.0126L$, is quite shallow, and the observed cavities

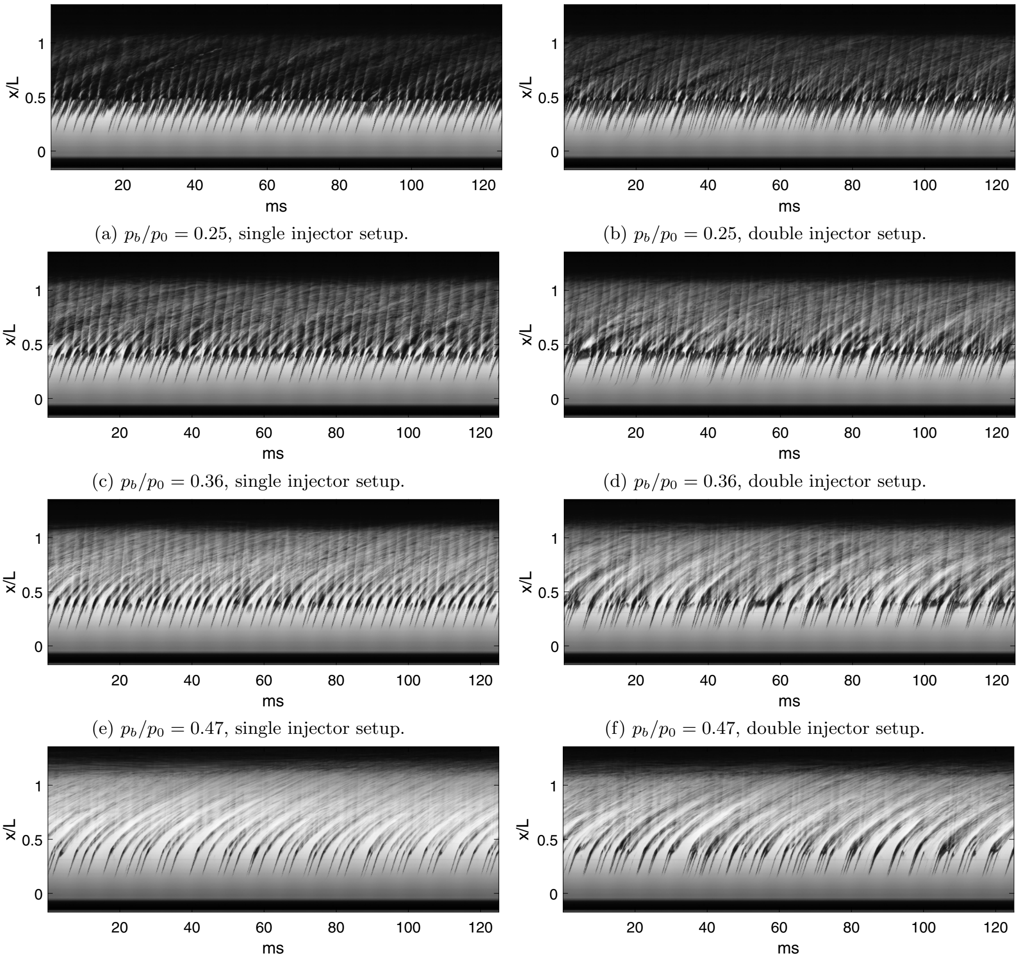

(a) $p_b/p_0 = 0.25$, single injector setup.

(b) $p_b/p_0 = 0.25$, double injector setup.

(c) $p_b/p_0 = 0.36$, single injector setup.

(d) $p_b/p_0 = 0.36$, double injector setup.

(e) $p_b/p_0 = 0.47$, single injector setup.

(f) $p_b/p_0 = 0.47$, double injector setup.

(g) $p_b/p_0 = 0.58$, single injector setup.

(h) $p_b/p_0 = 0.58$, double injector setup.

FIG. 13. Charts showing time history along nozzle center line ($t - x/L$) of 125 ms duration for aerated JP-5 for single (left) and double (right) injector setups at choked flow regime for outlet-inlet pressure ratios (from top to bottom): $p_b/p_0 = 0.25, 0.36, 0.47, 0.58$.

are very small, and there is no evidence of bright central regions due to transparent gas. Thus, we associate the higher intensity values to the liquid phase only and darker values to the gaseous phase. The grayscale imaging technique was assumed to be proportional to void fraction [28,48], which is justified under the uniform bubbly flow condition, as in our aerated cases. In our case, we use the following formula:

$$\alpha = (1 - C\langle I_{g+l}\rangle). \tag{C2}$$

Here $\langle I_{g+l}\rangle$ is the pixel intensity of the averaged mean flow field of each studied case, with bubbles and cavities in the flow, under identical light conditions between different experiments. We assume a simplified model where a linear relationship between the pixel intensity and the void fraction is assumed, with a constant coefficient C. The coefficient is obtained by calibration via computing the void fraction in the throat by Eq. (C1) and matching the void fraction in Eq. (C2) as illustrated in Fig. 15. We compute the time-averaged mean flow field for each choked flow regime case by averaging 1000 sequential frames (which corresponds to a 125 ms time window). In our study,

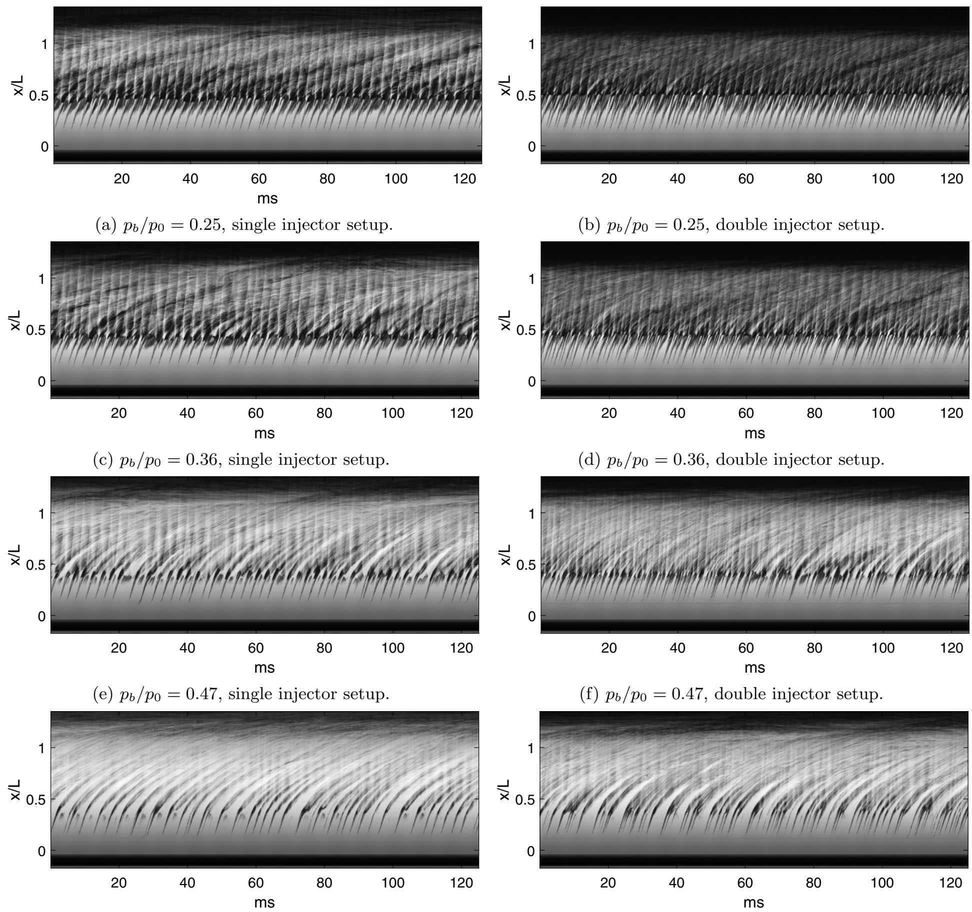

(a) $p_b/p_0 = 0.25$, single injector setup.
(b) $p_b/p_0 = 0.25$, double injector setup.
(c) $p_b/p_0 = 0.36$, single injector setup.
(d) $p_b/p_0 = 0.36$, double injector setup.
(e) $p_b/p_0 = 0.47$, single injector setup.
(f) $p_b/p_0 = 0.47$, double injector setup.
(g) $p_b/p_0 = 0.58$, single injector setup.
(h) $p_b/p_0 = 0.58$, double injector setup.

FIG. 14. Charts showing time history along nozzle center line ($t - x/L$) of 125 ms duration for aerated JP-8 for single (left) and double (right) injector setups at choked flow regime for outlet-inlet pressure ratios (from top to bottom): $p_b/p_0 = 0.25, 0.36, 0.47, 0.58$.

the pixel intensity varies in the range 0–1 and decreases due to the shades from the created cavity boundaries. By running experiments with a fully liquid state (without bubble injection and at higher back pressures, such that no cavities are created), we obtain the maximum intensity, I_l within different sections of the nozzle. This I_l is inversely related to the coefficient C, and our procedure yielded $C = 0.926/I_l = 1.02$ for JP-5, and $C = 0.915/I_l = 1.13$ for JP-8.

The grayscale method is applicable in our study for computing the void fraction in the diverging section in the aerated cases where the cavities uniformly populate the entire diverging section leading to spatially uniform grayscale values after averaging the images. The demonstrated strong similarity between our experimental data and nonlinear solutions of the governing equations as shown in Fig. 10 add further support to the validity of the used void fraction values obtained from the grayscale method in the aerated case. In contrast, the nonaerated cases did not satisfy this assumption, and for which application of the method is limited to the region of the attached cavity cloud. The overall void fraction uncertainty obtained using our grayscale method did not exceed $e_\alpha/\alpha = 10\%$ at the 95% confidence level for all aerated experiments in our study in the diverging section. For the throat region, where bubbles grow into larger gaseous voids, the maximum

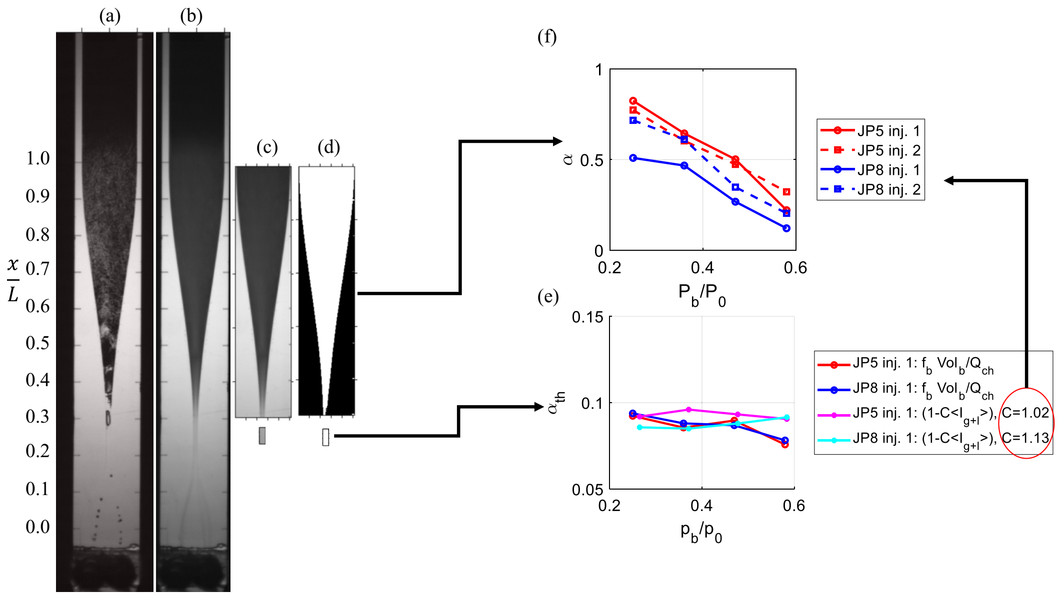

FIG. 15. Procedure to obtain void fraction estimates in the throat and outlet sections. (a) Instantaneous frame of JP-5 at $p_b/p_0 = 0.25$ (illustrated for two active bubble injectors). (b) Average frame is obtained by averaging 1000 instantaneous frames for each studied case. (c) The void fractions are obtained in two regions: the throat $x/L = 0.2$–0.25, and the diverging section $x/L = 0.25$–1. (d) The flow regions are masked, and the resulting masked field's average intensity is extracted. (e) The void void fractions in the nozzle throat. (f) The void fraction in the outlet, α, is obtained based on Eq. (C2).

uncertainty in the void fraction was $e_{\alpha_{th}}/\alpha_{th}$ =15%. Similar uncertainties were obtained in [2] using the grayscale method for the same nozzle and different liquids (including water, JP-8, and dodecane).

---

[1] R. F. Patella, J.-L. Reboud, and A. Archer, Cavitation damage measurement by 3D laser profilometry, Wear **246**, 59 (2000).

[2] P. F. Dunn, F. O. Thomas, M. P. Davis, and I. E. Dorofeeva, Experimental characterization of aviation-fuel cavitation, Phys. Fluids **22**, 117102 (2010).

[3] M. Dular and M. Martin Petkovsek, On the mechanisms of cavitation erosion—Coupling high speed videos to damage patterns, Exp. Therm. Fluid Sci. **68**, 359 (2015).

[4] K. Mørch, On the collapse of cavity clusters in flow cavitation, in *Cavitation and Inhomogeneities in Underwater Acoustics* (Springer, Berlin, Heidelberg, 1980), pp. 95–100

[5] G. Reisman, Y. C. Wang, and C. E. Brennen, Observations of shock waves in cloud cavitation, J. Fluid Mech. **355**, 255 (1998).

[6] C. E. Brennen, *Cavitation and Bubble Dynamics* (Cambridge University Press, Cambridge, 2014).

[7] K. Laberteaux and S. Ceccio, Partial cavity flows. Part 1. Cavities forming on models without spanwise variation, J. Fluid Mech. **431**, 1 (2001).

[8] R. B. Wade and A. J. Acosta, Experimental observations on the flow past a plano-convex hydrofoil, J. Basic Eng. **88**, 273 (1966).

[9] A. Kubota, H. Kato, and H. Yamaguchi, A new modelling of cavitating flows: A numerical study of unsteady cavitation on a hydrofoil section, J. Fluid Mech. **240**, 59 (1992).

[10] Y. Kawanami, H. Kato, H. Yamaguchi, M. Tanimura, and Y. Tagaya, Mechanism and control of cloud cavitation, J. Fluids Eng. **119**, 788 (1997).
[11] O. Coutier-Delgosha, J. F. Devillers, T. Pichon, A. Vabre, R. Woo, and S. Legoupil, Internal structure and dynamics of sheet cavitation, Phys. Fluids **18**, 017103 (2006).
[12] E. Grist, *Cavitation and the Centrifugal Pump: A Guide for Pump Users* (CRC Press, Boca Raton, FL, 1998).
[13] H. Chen, N. Doeller, Y. Li, and J. Katz, Experimental investigations of cavitation performance breakdown in an axial waterjet pump, J. Fluids Eng. **142**, 091204 (2020).
[14] H. Ganesh, S. A. Mäkiharju, and S. L. Ceccio, Bubbly shock propagation as a mechanism for sheet-to-cloud transition of partial cavities, J. Fluid Mech. **802**, 37 (2016).
[15] P. Tomov, S. Khelladi, F. Ravelet, C. Sarraf, F. Bakir, and P. Vertenoeuil, Experimental study of aerated cavitation in a horizontal venturi nozzle, Exp. Therm. Fluid Sci. **70**, 85 (2016).
[16] S. Jahangir, W. Hogendoorn, and C. Poelma, Dynamics of partial cavitation in an axisymmetric converging-diverging nozzle, Int. J. Multiphase Flow **106**, 34 (2018).
[17] M. Brunhart, C. Soteriou, M. Gavaises, I. Karathanassis, P. Koukouvinis, S. Jahangir, and C. Poelma, Investigation of cavitation and vapor shedding mechanisms in a venturi nozzle, Phys. Fluids **32**, 083306 (2020).
[18] A. Gnanaskandan and K. Mahesh, Large eddy simulation of the transition from sheet to cloud cavitation over a wedge, Int. J. Multiphase Flow **83**, 86 (2016).
[19] T. Trummler, S. Schmidt, and N. A. Adams, Investigation of condensation shocks and re-entrant jet dynamics in a cavitating nozzle flow by large-eddy simulation, Int. J. Multiphase Flow **125**, 103215 (2020).
[20] L. Noordzij and L. Van Wijngaarden, Relaxation effects, caused by relative motion, on shock waves in gas-bubble/liquid mixtures, J. Fluid Mech. **66**, 115 (1974).
[21] L. d'Agostino and C. E. Brennen, *On the Acoustical Dynamics of Bubble Clouds* (ASME Cavitation and Multiphase Flow Forum, 1983).
[22] M. Kameda and Y. Matsumoto, Shock waves in a liquid containing small gas bubbles, Phys. Fluids **8**, 322 (1996).
[23] H. Shamsborhan, O. Coutier-Delgosha, G. Caignaert, and F. A. Nour, Experimental determination of the speed of sound in cavitating flows, Exp. Fluids **49**, 1359 (2010).
[24] S. A. Mäkiharju, H. Ganesh, and S. L. Ceccio, The dynamics of partial cavity formation, shedding and the influence of dissolved and injected non-condensable gas, J. Fluid Mech. **829**, 420 (2017).
[25] I.-H. Lee, S. A. Mäkiharju, H. Ganesh, and S. L. Ceccio, Scaling of gas diffusion into limited partial cavities, J. Fluids Eng. **138**, 051301 (2016).
[26] Z. Dong and P. Su, Cavitation control by aeration and its compressible characteristics, J. Hydrodynam. **18**, 499 (2006).
[27] F. Brandao, M. Bhatt, and K. Mahesh, Effects of non-condensable gas on cavitating flow over a cylinder, in *Proceedings of the 10th International Symposium on Cavitation*, edited by J. Katz (ASME Press, New York, 2018).
[28] C. Wang, B. Huang, M. Zhang, G. Wang, Q. Wu, and D. Kong, Effects of air injection on the characteristics of unsteady sheet/cloud cavitation shedding in the convergent-divergent channel, Int. J. Multiphase Flow **106**, 1 (2018).
[29] F. L. Brandao, M. Bhatt, and K. Mahesh, Numerical study of cavitation regimes in flow over a circular cylinder, J. Fluid Mech. **885**, A19 (2020).
[30] H. Cheng, X. Long, B. Ji, X. Peng, and M. Farhat, A new Euler-Lagrangian cavitation model for tip-vortex cavitation with the effect of non-condensable gas, Int. J. Multiphase Flow **134**, 103441 (2021).
[31] CRC, *Handbook of Aviation Fuel Properties*, 530 (The Council, 1983).
[32] J. T. Edwards, Jet fuel properties, Technical Report, Air Force Research Laboratory Wright-Patterson AFB (2020).
[33] P. F. Dunn, F. O. Thomas, J. B. Leighton, and Lv D., Determination of Henry's law constant and the diffusion and polytropic coefficients of air in aviation fuel, Fuel **90**, 1257 (2011).

[34] I. Dorofeeva, F. Thomas, and P. Dunn, Cavitation of JP-8 fuel in a converging-diverging nozzle: Experiments and modeling, in *Proceedings of the 7th International Symposium on Cavitation* (Ann Arbor, Michigan, 2009), pp. 854–863.

[35] M. Waldrop and F. Thomas, Aviation fuel cavitation in a CD nozzle: A quantitative experimental characterization, in *Proceedings of the 10th International Symposium on Cavitation (CAV2018)* (ASME Press, New York, 2018).

[36] A. T. Preston, T. Colonius, and C. E. Brennen, A numerical investigation of unsteady bubbly cavitating nozzle flows, Phys. Fluids **14**, 300 (2002).

[37] M. T. Waldrop, Experimental characterization and modeling of gaseous cavitation of dodecane in a converging-diverging nozzle, Ph.D. thesis, University of Notre Dame (2020).

[38] B. R. Sutherland, S. B. Dalziel, G. O. Hughes, and P. F. Linden, Visualization and measurement of internal waves by 'synthetic schlieren'. Part 1. Vertically oscillating cylinder, J. Fluid Mech. **390**, 93 (1999).

[39] S. Dalziel, G. O. Hughes, and B. R. Sutherland, Whole-field density measurements by 'synthetic schlieren', Exp. Fluids **28**, 322 (2000).

[40] G. S. Settles, *Schlieren and Shadowgraph Techniques: Visualizing Phenomena in Transparent Media* (Springer Science & Business Media, 2001).

[41] See Supplemental Material at http://link.aps.org/supplemental/10.1103/PhysRevFluids.7.084305 for details see ReadmeSupplemnetalMaterial.txt file.

[42] B. Ran and J. Katz, Pressure fluctuations and their effect on cavitation inception within water jets, J. Fluid Mech. **262**, 223 (1994).

[43] I. Gluzman and F. O. Thomas, Characterization of bubble dynamics in the nozzle flow of aviation fuels via computer vision tools, Int. J. Multi. Flow **154**, 104133 (2022).

[44] J. Leandro, R. Carvalho, Y. Chachereau, and H. Chanson, Estimating void fraction in a hydraulic jump by measurements of pixel intensity, Exp. Fluids **52**, 1307 (2012).

[45] J. Leandro, D. B. Bung, and R. Carvalho, Measuring void fraction and velocity fields of a stepped spillway for skimming flow using non-intrusive methods, Exp. Fluids **55**(5), 1732 (2014).

[46] N. Mitroglou, M. Lorenzi, M. Santini, and M. Gavaises, Application of x-ray micro-computed tomography on high-speed cavitating diesel fuel flows, Exp. Fluids **57**, 175 (2016).

[47] A. Dash, S. Jahangir, and C. Poelma, Direct comparison of shadowgraphy and x-ray imaging for void fraction determination, Meas. Sci. Technol. **29**, 125303 (2018).

[48] I. Biluš, G. Bombek, M. Hočevar, B. Širok, T. Cenčič, and M. Petkovšek, The experimental analysis of cavitating structure fluctuations and pressure pulsations in the cavitation station, Strojniški vestnik–J. Mech. Eng. **60**, 147 (2014).